

Four- and six-photon stimulated Raman transitions for coherent qubit and qudit operations

G. J. Gregory*, E. R. Ritchie, A. Quinn, S. Brudney, D. J. Wineland, D. T. C. Allcock, and J. O'Reilly*
Department of Physics, University of Oregon, Eugene, OR, USA
 (Dated: Tuesday 24th February, 2026)

We experimentally demonstrate transitions between electronic angular momentum states with a difference in magnetic quantum numbers $\Delta m_J = 3, 4,$ and 5 via resonant four- and six-photon stimulated Raman transitions in a single trapped atom. Derivation of the corresponding Rabi frequencies, which are verified experimentally, follows the standard treatment of two-photon transitions including the adiabatic elimination of intermediate states. Finally, we discuss pathways to increase the observed multi-photon transition fidelities to $> 99.99\%$, providing a tool for efficient, high-fidelity control of qudits and single-atom logical qubits.

Two-photon stimulated Raman transitions are a well-developed tool for unitary control over qubits encoded in trapped ions [1], neutral atoms [2, 3], solid state systems [4, 5], and molecules [6]. They can be deployed in large-scale systems with absolute phase stability in space and time [7] and allow for individual addressing of qubits [8]. Their implementation has enabled sub- μs quantum logic gate operations [9] and single and two-qubit gate fidelities in trapped ions exceeding 99.99% and 99.9%, respectively [10, 11]. In addition to computing, two-photon stimulated Raman transitions have also found uses in matter-wave interferometry [12, 13] and quantum simulation [14]. These transitions typically consist of simultaneous absorption and emission of single photons via electric dipole transitions and thus are limited to coupling quantum states with a difference of at most two units of angular momentum.

There has been growing interest in encoding quantum information within the higher-dimensional Hilbert spaces native to atomic systems [15–18]. So-called qudit encodings (with dimension $d > 2$) have been shown to simplify circuits [19] and tomography [20] and enable efficient quantum simulation of higher-dimensional physical systems [21, 22]. Numerical simulations have also shown more efficient error correction using qudits [23], with experimental implementations of codes embedded in single ion qudits recently demonstrating better-than-physical performance [24, 25]. While some implementations have maximized dimension by encoding computational states in both metastable and ground manifolds [15–17], metastable-only encodings enable the conversion of almost all leakages out of the qudit subspace into erasure errors [26, 27] while still providing a large Hilbert space [28]. This feature has been shown to reduce the overhead of fault tolerant quantum error correction in numerical simulations [29, 30]. In addition, metastable encodings are compatible with same-species sympathetic cooling

and mid-circuit readout [31, 32], thus reducing experimental complexity.

Large metastable qudit encodings inevitably contain state pairs with $|\Delta m| > 2$ or $|\Delta F| > 2$ that consequently cannot be directly coupled with dipole-based two-photon processes [33], so realizing some unitaries will require longer sequences of pulses coupling to intermediate qudit states. Specific examples include logical operations in \mathbb{A} [34] and other single-atom quantum error correction codes [35]. This can be mitigated to some extent by driving sequences of single-photon electric quadrupole transitions, but these are temperature sensitive, reliant on narrow-linewidth lasers, and not straightforwardly compatible with same-species sympathetic cooling. Multi-photon quadrupole transitions could in principle bypass some of these limitations but may be slow and to the best of our knowledge have not been demonstrated.

To bridge this gap, we propose to use $2n$ -photon stimulated Raman transitions to directly couple states separated by up to $2n$ units of angular momentum. Four-photon Raman processes have previously been observed in ensembles of neutral atoms [36, 37] and carbon nanotubes [38], but not in individual atomic systems with high-fidelity state transfer and readout. In one study, fifty-photon Raman transitions were demonstrated with high efficiency for a $d = 2$ system in a gas of Rb atoms [39]. More common examples of multi-photon processes include four-wave mixing in cold atom ensembles [40], which generally involves four separate manifolds, and Bragg diffraction for matter wave interferometers [13], which does not change the internal state. Neither technique, to the best of our knowledge, has been directly incorporated into quantum information processing. Four-photon ac Stark shifts have been measured in trapped ions [41, 42], but a detailed study of higher order processes driving coherent population transfer within an

isolated manifold has not yet been put forth.

In this Letter, we present a theoretical treatment and experimental verification of stimulated Raman transitions driven by four- and six-photon processes capable of directly coupling state pairs with $|\Delta m_J| > 2$. We derive analytic formulas for the corresponding Rabi frequencies and verify them for specific transitions with $|\Delta m_J| = 3$ and $|\Delta m_J| = 4$ in the $D_{5/2}$ metastable manifold of a single trapped $^{40}\text{Ca}^+$ ion. We achieve four- and six-photon π -pulse transfer fidelities of 96(1)% and 78(4)% and discuss the path towards decreasing the infidelities below 10^{-4} . Finally, we drive select $\Delta m_J > 2$ transitions that enable full state-to-state connectivity of a metastable qudit in the $D_{5/2}$ manifold, providing a potential pathway towards more efficient Raman-based qudit control.

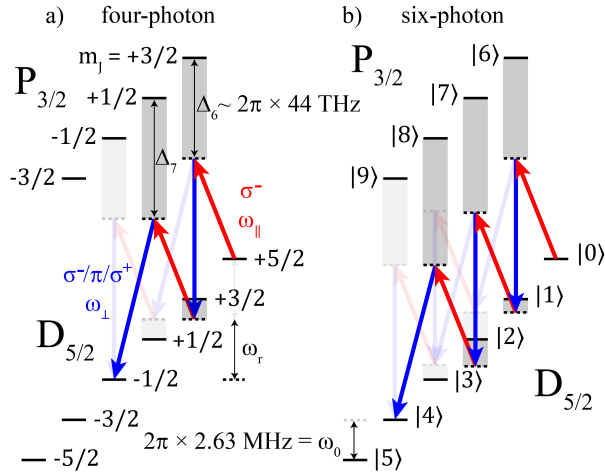


FIG. 1. **a)** Illustration of four-photon transition pathways between $|0\rangle \equiv |m_J = +5/2\rangle$ and $|3\rangle \equiv |m_J = -1/2\rangle$ in the $D_{5/2}$ manifold of $^{40}\text{Ca}^+$. They are driven by two 976 nm beams with σ^- (red) and equal components of σ^+ , π and σ^- (blue) polarizations and a relative detuning ω_r . **b)** Six-photon transition between $|0\rangle$ and $|4\rangle$. Solid and transparent lines represent (three of the five) interfering pathways that drive the multi-photon transitions, with solid lines highlighted as an example pathway. Energies are not to scale.

For concreteness, we present derivations of four- and six-photon processes within the $D_{5/2}$ manifold of $^{40}\text{Ca}^+$, but the underlying physics can be straight-forwardly extended to other systems. The Zeeman structure of the first excited metastable $D_{5/2}$ and short-lived $P_{3/2}$ manifolds (lifetimes of 1.168(7) s [43] and 6.64(4) ns [44], respectively) are shown in Fig. 1, with metastable levels split by $\omega_0 = 2\pi \times 2.63$ MHz due to a quantization field of ~ 1.56 G.

We consider dynamics driven by two beams far-

detuned by Δ from the $D_{5/2} \leftrightarrow P_{3/2}$ resonance. One beam (R_{\parallel}) we assume to be aligned with the magnetic field with nominally pure σ^- polarization and a frequency ω_{\parallel} (red in Fig. 1). The other beam (R_{\perp}) propagates orthogonally to the magnetic field with frequency ω_{\perp} and contains approximately equal components of σ^+ , π and σ^- polarized light (blue in Fig. 1). For an n -photon transition between states $|i\rangle$ and $|j\rangle$, the relative beam detuning $\omega_r \equiv \omega_{\perp} - \omega_{\parallel}$ is set to satisfy the resonance condition

$$\omega_r = \frac{2|E_i - E_j|}{n\hbar}. \quad (1)$$

The interaction of a laser field with states $|i\rangle$ and $|j\rangle$ is expressed by the ij 'th component of the interaction Hamiltonian

$$H_{ij} = -\frac{\hbar}{2}\Omega_{ij}e^{-i\omega t} \quad (2)$$

where Ω_{ij} is the complex single-photon Rabi frequency and ω is the laser frequency.

We present in SM B two separate approaches to derive effective higher order Rabi frequencies. The first follows a straight forward derivation of the two-photon Raman Rabi frequency [1], wherein state amplitude equations of motion are generated via the Schrödinger equation. In the second treatment, we invoke time-dependent perturbation theory and calculate the lowest order corrections to the time evolution propagator.

In the standard treatment of two-photon Raman transitions [1], the single-beam detuning Δ is taken to be much larger than the time derivative of the excited state's corresponding complex amplitude. Under that assumption, the state may be adiabatically eliminated, uncoupling the equations of motion and reducing the problem to an effective two-state system. The key approximation that we make in both treatments is that the MHz-scale detuning from intermediate states within the $D_{5/2}$ is enough to adiabatically eliminate those states as well.

Using state labels defined in Fig. 1, we thus find the four- and six-photon Rabi frequencies

$$\Omega_{03}^{(4)} = \frac{\Omega_{06}^*}{8\Delta^2} \left(\frac{\Omega_{16}\Omega_{17}^*\Omega_{37}}{\omega_r - \omega_{01}} - \frac{\Omega_{26}\Omega_{28}^*\Omega_{38}}{\omega_r - \omega_{23}} \right) \quad (3)$$

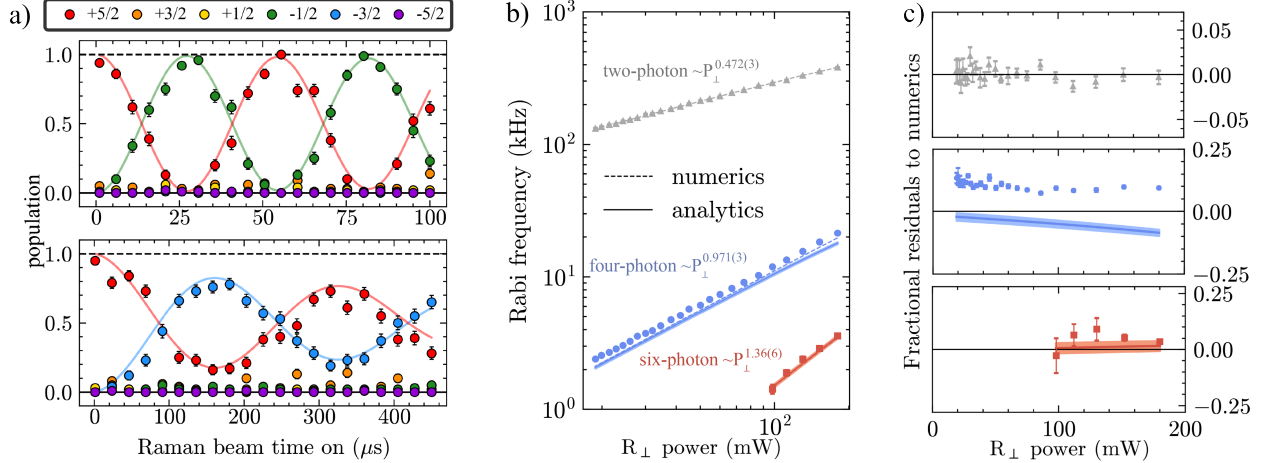


FIG. 2. **a)** (Top) Rabi-flopping driven by the resonant four-photon process displayed in Fig. 1a. (Bottom) Rabi flopping driven by the six-photon resonant transition shown in Fig. 1b. **b)** Two- (gray), four- (blue) and six-photon (red) transition Rabi frequencies as a function of R_{\perp} beam power, with R_{\parallel} held fixed at 195 mW. Blue and red solid lines correspond to the predictions of Equations (3) and (4), respectively, plus corrections for F-state couplings and polarization impurities (see SM E and F). Shaded regions represent 68% confidence intervals from fits to beam intensities and polarizations. Dashed lines are predictions from numerical simulations. **c)** Fractional residuals of data and analytic predictions (colored curves) to numeric predictions of the Rabi frequencies.

$$\begin{aligned}
 \Omega_{04}^{(6)} = \frac{\Omega_{06}^*}{32\Delta^3} & \left(\frac{\Omega_{16}\Omega_{17}^*\Omega_{27}\Omega_{28}^*\Omega_{48}}{(\omega_r - \omega_{01})(2\omega_r - \omega_{02})} \right. \\
 & - \frac{\Omega_{16}\Omega_{17}^*\Omega_{37}\Omega_{39}^*\Omega_{49}}{(\omega_r - \omega_{01})(\omega_{03} - 2\omega_r)} \\
 & + \frac{\Omega_{26}\Omega_{28}^*\Omega_{38}\Omega_{39}^*\Omega_{49}}{(\omega_{02} - \omega_r)(\omega_{03} - 2\omega_r)} \\
 & - \frac{\Omega_{26}\Omega_{28}^*\Omega_{28}\Omega_{28}^*\Omega_{48}}{(\omega_{02} - \omega_r)(2\omega_r - \omega_{02})} \\
 & \left. + \frac{\Omega_{06}\Omega_{06}^*\Omega_{26}\Omega_{28}^*\Omega_{48}}{\omega_r(2\omega_r - \omega_{02})} \right) \quad (4)
 \end{aligned}$$

where ω_{ij} is the angular frequency splitting between states $|i\rangle$ and $|j\rangle$ including corrections due to ac Stark shifts induced by the R_{\parallel} and R_{\perp} beams. Each term in Equations (3) and (4) corresponds to one of the resonant pathways drawn in Fig. 1. We find convergence between these equations and numerical simulations of the full $D_{5/2}$ interaction Hamiltonian detailed in SM C. In general, ignoring interference between different pathways, the two-, four-, and six-photon transition Rabi frequencies scale as

$$\Omega^{(2-photon)} \propto \frac{\Omega^2}{\Delta} \quad (5)$$

$$\Omega^{(4-photon)} \propto \frac{\Omega^4}{\Delta^2\omega_0} \quad (6)$$

$$\Omega^{(6-photon)} \propto \frac{\Omega^6}{\Delta^3\omega_0^2} \quad (7)$$

which corresponds to $(P_{\perp}P_{\parallel})^{n/4}$ scaling with the beam powers for n -photon transitions.

To validate these predictions, we performed experiments with a single trapped and laser-cooled ion driven by 976 nm stimulated Raman transition laser beams with $\Delta = -2\pi \times 44$ THz. To prepare the ion in an arbitrary sublevel of the $D_{5/2}$ manifold, we first Doppler and electromagnetically-induced transparency (EIT) cool [45] its motion to $\bar{n} < 1$ and then optically pump it to the $|S_{1/2}, m_J = +1/2\rangle$ state using 397 nm and 866 nm laser beams. Then, we drive a narrow, state-selective, 729 nm $S_{1/2} \leftrightarrow D_{5/2}$ electric quadrupole transition preceded by an optional rf π pulse to $|S_{1/2}, m_J = -1/2\rangle$. After this shelving process [46], we perform a fluorescence check for 500 μ s and repeat the process until the ion is dark, indicating successful preparation in $D_{5/2}$ [47].

We read out each sublevel of the $D_{5/2}$ manifold by deshelving them in turn to the $S_{1/2}$ manifold and checking for fluorescence on the 397 nm cycling transition with the 866 nm repumping beam on. The first state to produce a bright signal is considered the measurement result, but imperfect deshelving pulses can lead to the ion remaining dark through all the checks. These shots are discarded and lead to a qudit readout inefficiency of $\sim 0.5\%$. For the remaining trials we achieve state preparation and measurement fidelities above 99.5% for all states within the $D_{5/2}$ manifold.

Each 976 nm beam is focused to a ~ 30 μ m waist at

the ion, and the power in the R_{\parallel} beam is held constant at 195 mW while the power in the R_{\perp} beam is varied from 20 - 180 mW to probe dynamics at different timescales. At each beam power setting, we perform Rabi spectroscopy of the two transitions and then measure resonant driving as shown in Fig. 2a with 195 and 152 mW in the R_{\parallel} and R_{\perp} beams, respectively. To extract a Rabi frequency from the damped oscillations, we fit to a magnetic field noise model described in SM D.

We calibrate the intensity in each polarization component of the R_{\parallel} and R_{\perp} beams by performing auxiliary measurements including the two-photon $m_J = +5/2 \leftrightarrow +3/2$ transition Rabi frequency at different R_{\perp} beam powers (see SM E). We find good agreement between the measured four- and six-photon Rabi frequencies, the converging analytic predictions given by equations (3) and (4), and numerical simulations, all shown in Fig. 2, including small corrections due to polarization impurities and couplings to F manifold states (see SM F). The remaining discrepancy between the measured and predicted four-photon Rabi frequencies is most likely caused by a miscalibration of the beam parameters, potentially due to an uncompensated ac Zeeman shift.

The contrast of the four-photon Rabi flops, corresponding to a π pulse transfer fidelity from $|0\rangle$ to $|3\rangle$, is limited by two dominant mechanisms presented in Fig. 3. At low beam powers, ambient magnetic field fluctuations significantly damp the Rabi oscillations, while at high beam powers we observe measurable population of the intermediate states with fast, MHz-scale oscillations. We numerically simulate resonant dynamics of the six-level system and set the maximum total population in the intermediate states as an upper bound on the infidelity. Experimentally, we achieve a maximal four-photon π pulse transfer fidelity of 96(1)% at 48.6(3) μ s, with fidelity limitations in the fast and slow π time regimes in line with predictions considering the two dominant error sources.

These results can be greatly improved, potentially to a level competitive with the best two-photon stimulated Raman gates [49], by implementing well-known techniques including magnetic field stabilization [48] and pulse shaping (see SM H). Square pulses, like we used in these experiments, have significant frequency components at the intermediate state two-photon resonances. If we instead ramp the beam intensities on and off, with \sin^2 given as an example in Fig. 3, the power spectral density (PSD) at the intermediate state frequencies is reduced and the off-resonant driving amplitudes ramp down with the

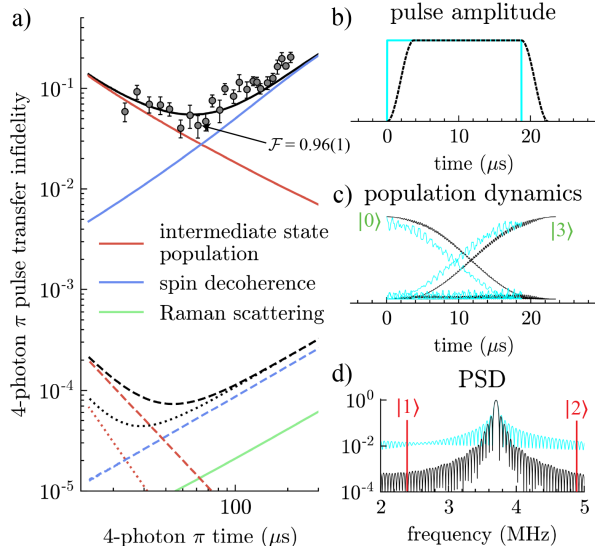


FIG. 3. **a)** Four-photon π pulse transfer infidelity at different four-photon π times, corresponding to different R_{\perp} beam powers, with expected contributions due to intermediate state population (solid red), spin decoherence (solid blue), and spontaneous Raman scatter error (solid green). Solid black line represents the sum of each expected contribution. Dashed blue line is projected spin dephasing infidelity with coherence demonstrated in [48]. Dashed and dotted red lines are the numerically-simulated maximum leakage to intermediate states with the R_{\perp} beam amplitude ramped with \sin^2 and \sin^4 envelopes respectively. **b)** Two-beam pulse envelopes with R_{\perp} amplitude without pulse shaping (black) and shaped with a \sin^2 ramp (cyan). **c)** Numerically simulated resonant population dynamics driven by pulses shown in b). **d)** Power spectral density of pulses in b).

intensity, leading to a much more robust transfer to the target state.

The total expected infidelity incurred by spin dephasing, spontaneous Raman scattering, and population of the intermediate states can thus be reduced below the 10^{-4} level at reasonable π times. In principle, there does not appear to be anything fundamental preventing four- and six-photon single qubit gates from achieving fidelities demonstrated in state-of-the-art two-photon gates. Additionally, the intensity sensitivity of four-photon transitions should be of the same order as Raman-driven Mølmer-Sørensen entangling gates, so we expect the intensity stabilization requirements to be equivalent to previously demonstrated capabilities [10]. We note that the use of two non-copropagating beams in this work was to maximize the available intensity and is not strictly necessary.

In Fig. 4a we present spectroscopy of additional

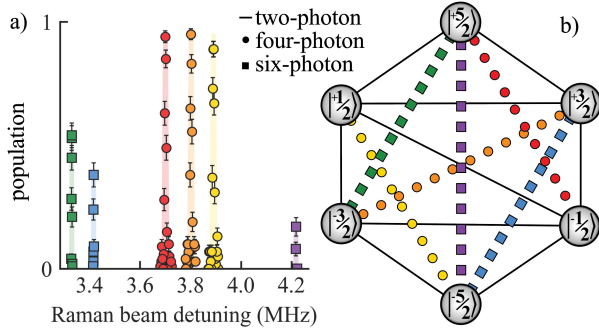


FIG. 4. **a)** Rabi spectroscopy of transitions within $D_{5/2}$ with $\Delta m_J \geq 3$ as driven by four (circles) and six (squares) photon processes. **b)** Diagram illustrating full direct unitary connectivity in the $D_{5/2}$ manifold enabled by four- and six-photon transitions.

four- and six-photon transitions that enable full state-to-state connectivity in the $D_{5/2}$ manifold, with spectral isolation of each transition provided by R_{\parallel} -induced ac Stark shifts. This connectivity is illustrated in Fig. 4b, with transitions driven by two, four, and six photon processes marked with lines, circles, and squares, respectively.

These transitions can provide arbitrary unitary control between qudit states with a clear path to fidelities in excess of 99.99%, which will enable more efficient qudit control, state tomography, and simplified direct unitaries in single-atom quantum error correction codes like the absorption-emission code [34] and spin-cat logical encodings [24, 35]. Additionally, the $(P_{\perp}P_{\parallel})^{n/4}$ scaling of n -photon transition Rabi frequencies can be exploited to reduce cross-talk in individually addressed atom arrays [39]. With growing interest in and emerging demonstrations of higher-dimensional quantum information processing, we believe that the implementation of high-fidelity four- and six-photon transitions may provide a useful tool towards achieving fault-tolerant quantum computing with a lower hardware overhead.

Acknowledgments — We acknowledge useful discussions with K. Barajas, W. Campbell, E. Hudson, K. DeBry, I. Chuang, J. Chiaverini, V. Buchemavari, D. Slichter, and H. Häeffner. This research is supported in part by the NSF through the QSEnSE Quantum Leap Challenge Institute, Award #2016244 and the US Army Research Office under award W911NF-24-1-0379. The data supporting the figures in this article are available upon reasonable request from J.O.

* Corresponding authors: ggregory@uoregon.edu; joreilly@uoregon.edu

- [1] D. Leibfried, R. Blatt, C. Monroe, and D. Wineland, Quantum dynamics of single trapped ions, *Rev. Mod. Phys.* **75**, 281 (2003).
- [2] D. D. Yavuz, P. B. Kulatunga, E. Urban, T. A. Johnson, N. Proite, T. Henage, T. G. Walker, and M. Saffman, Fast ground state manipulation of neutral atoms in microscopic optical traps, *Phys. Rev. Lett.* **96**, 063001 (2006).
- [3] M. P. A. Jones, J. Beugnon, A. Gaëtan, J. Zhang, G. Messin, A. Browaeys, and P. Grangier, Fast quantum state control of a single trapped neutral atom, *Phys. Rev. A* **75**, 040301 (2007).
- [4] M. L. Goldman, T. L. Patti, D. Levonian, S. F. Yelin, and M. D. Lukin, Optical control of a single nuclear spin in the solid state, *Phys. Rev. Lett.* **124**, 153203 (2020).
- [5] C. G. Yale, B. B. Buckley, D. J. Christle, G. Burkard, F. J. Heremans, L. C. Bassett, and D. D. Awschalom, All-optical control of a solid-state spin using coherent dark states, *Proceedings of the National Academy of Sciences* **110**, 7595 (2013).
- [6] U. Gaubatz, P. Rudecki, S. Schiemann, and K. Bergmann, Population transfer between molecular vibrational levels by stimulated raman scattering with partially overlapping laser fields. a new concept and experimental results, *The Journal of Chemical Physics* **92**, 5363 (1990), https://pubs.aip.org/aip/jcp/article-pdf/92/9/5363/18986309/5363_1_online.pdf.
- [7] I. V. Inlek, G. Vittorini, D. Hucul, C. Crocker, and C. Monroe, Quantum gates with phase stability over space and time, *Phys. Rev. A* **90**, 042316 (2014).
- [8] H. Häffner, W. Hänsel, C. F. Roos, J. Benhelm, D. Chek-al kar, M. Chwalla, T. Körber, U. D. Rapol, M. Riebe, P. O. Schmidt, C. Becher, O. Gühne, W. Dür, and R. Blatt, Scalable multiparticle entanglement of trapped ions, *Nature* **438**, 643–646 (2005).
- [9] V. M. Schäfer, C. J. Ballance, K. Thirumalai, L. J. Stephenson, T. G. Ballance, A. M. Steane, and D. M. Lucas, Fast quantum logic gates with trapped-ion qubits, *Nature* **555**, 75 (2018).
- [10] J. P. Gaebler, T. R. Tan, Y. Lin, Y. Wan, R. Bowler, A. C. Keith, S. Glancy, K. Coakley, E. Knill, D. Leibfried, and D. J. Wineland, High-fidelity universal gate set for $^9\text{Be}^+$ ion qubits, *Phys. Rev. Lett.* **117**, 060505 (2016).
- [11] C. J. Ballance, T. P. Harty, N. M. Linke, M. A. Sepiol, and D. M. Lucas, High-fidelity quantum logic gates using trapped-ion hyperfine qubits, *Phys. Rev. Lett.* **117**, 060504 (2016).
- [12] M. Kasevich and S. Chu, Atomic interferometry using stimulated raman transitions, *Phys. Rev. Lett.* **67**, 181 (1991).
- [13] H. Müller, S.-w. Chiow, Q. Long, S. Herrmann, and S. Chu, Atom interferometry with up to 24-photon-momentum-transfer beam splitters, *Phys. Rev. Lett.*

- 100**, 180405 (2008).
- [14] C. Monroe, W. C. Campbell, L.-M. Duan, Z.-X. Gong, A. V. Gorshkov, P. W. Hess, R. Islam, K. Kim, N. M. Linke, G. Pagano, P. Richerme, C. Senko, and N. Y. Yao, Programmable quantum simulations of spin systems with trapped ions, *Rev. Mod. Phys.* **93**, 025001 (2021).
- [15] P. Hrmo, B. Wilhelm, L. Gerster, M. W. van Mourik, M. Huber, R. Blatt, P. Schindler, T. Monz, and M. Ringbauer, Native qudit entanglement in a trapped ion quantum processor, *Nature Communications* **14**, 2242 (2023).
- [16] Z. Jia, W. Huie, L. Li, W. K. C. Sun, X. Hu, Aakash, H. Kogan, A. Karve, J. Y. Lee, and J. P. Covey, An architecture for two-qubit encoding in neutral ytterbium-171 atoms, *npj Quantum Information* **10**, 106 (2024).
- [17] P. J. Low, B. White, and C. Senko, Control and readout of a 13-level trapped ion qudit, *npj Quantum Information* **11**, 85 (2025).
- [18] E. O. Kiktenko, A. S. Nikolaeva, and A. K. Fedorov, Colloquium: Qudits for decomposing multi-qubit gates and realizing quantum algorithms, *Rev. Mod. Phys.* **97**, 021003 (2025).
- [19] B. P. Lanyon, M. Barbieri, M. P. Almeida, T. Jennewein, T. C. Ralph, K. J. Resch, G. J. Pryde, J. L. O'Brien, A. Gilchrist, and A. G. White, Simplifying quantum logic using higher-dimensional hilbert spaces, *Nat. Phys.* **5**, 134 (2009).
- [20] R. Stricker, M. Meth, L. Postler, C. Edmunds, C. Ferrie, R. Blatt, P. Schindler, T. Monz, R. Kueng, and M. Ringbauer, Experimental single-setting quantum state tomography, *PRX Quantum* **3**, 040310 (2022).
- [21] D. González-Cuadra, T. V. Zache, J. Carrasco, B. Kraus, and P. Zoller, Hardware efficient quantum simulation of non-abelian gauge theories with qudits on rydberg platforms, *Phys. Rev. Lett.* **129**, 160501 (2022).
- [22] C. Senko, P. Richerme, J. Smith, A. Lee, I. Cohen, A. Retzker, and C. Monroe, Realization of a quantum integer-spin chain with controllable interactions, *Phys. Rev. X* **5**, 021026 (2015).
- [23] F. H. E. Watson, H. Anwar, and D. E. Browne, Fast fault-tolerant decoder for qubit and qudit surface codes, *Phys. Rev. A* **92**, 032309 (2015).
- [24] K. DeBry, N. Meister, A. V. Martinez, C. D. Bruzewicz, X. Shi, D. Reens, R. McConnell, I. L. Chuang, and J. Chiaverini, Error correction of a logical qubit encoded in a single atomic ion (2025), arXiv:2503.13908.
- [25] Y. Li, Q. Mei, Q.-X. Jie, W. Cai, Y. Li, Z. Liu, Z.-J. Chen, Z. Xie, X. Cheng, X. Zhao, Z. Luo, M. Zhang, X.-B. Zou, C.-L. Zou, Y. Lin, and J. Du, Beating the break-even point with autonomous quantum error correction (2025), arXiv:2504.16746.
- [26] A. Quinn, G. J. Gregory, I. D. Moore, S. Brudney, J. Metzner, E. R. Ritchie, J. O'Reilly, D. J. Wineland, and D. T. C. Allcock, High-fidelity entanglement of metastable trapped-ion qubits with integrated erasure conversion (2024), arXiv:2411.12727.
- [27] X. Shi, J. Sinanan-Singh, K. DeBry, S. L. Toldaro, I. L. Chuang, and J. Chiaverini, Long-lived metastable-qubit memory, *Physical Review A* **111**, L020601 (2025).
- [28] X. Shi, J. Sinanan-Singh, T. J. Burke, J. Chiaverini, and I. L. Chuang, Efficient implementation of a quantum algorithm with a trapped ion qudit (2025).
- [29] Y. Wu, S. Kolkowitz, S. Puri, and J. D. Thompson, Erasure conversion for fault-tolerant quantum computing in alkaline earth rydberg atom arrays, *Nature Communications* **13**, 10.1038/s41467-022-32094-6 (2022).
- [30] M. Kang, W. C. Campbell, and K. R. Brown, Quantum error correction with metastable states of trapped ions using erasure conversion, *PRX Quantum* **4**, 020358 (2023).
- [31] D. T. C. Allcock, W. C. Campbell, J. Chiaverini, I. L. Chuang, E. R. Hudson, I. D. Moore, A. Ransford, C. Roman, J. M. Sage, and D. J. Wineland, omg blueprint for trapped ion quantum computing with metastable states, *Applied Physics Letters* **119**, 10.1063/5.0069544 (2021).
- [32] H.-X. Yang, J.-Y. Ma, Y.-K. Wu, Y. Wang, M.-M. Cao, W.-X. Guo, Y.-Y. Huang, L. Feng, Z.-C. Zhou, and L.-M. Duan, Realizing coherently convertible dual-type qubits with the same ion species, *Nature Physics* **18**, 1058 (2022).
- [33] P. J. Low, N. C. F. Zutt, G. A. Tathed, and C. Senko, Quantum logic operations and algorithms in a single 25-level atomic qudit (2025), arXiv:2507.15799.
- [34] S. P. Jain, E. R. Hudson, W. C. Campbell, and V. V. Albert, Absorption-emission codes for atomic and molecular quantum information platforms, *Phys. Rev. Lett.* **133**, 260601 (2024).
- [35] S. Omanakuttan, V. Buchemavari, J. A. Gross, I. H. Deutsch, and M. Marvian, Fault-tolerant quantum computation using large spin-cat codes, *PRX Quantum* **5**, 020355 (2024).
- [36] Z. Fu, P. Wang, S. Chai, L. Huang, and J. Zhang, Bose-einstein condensate in a light-induced vector gauge potential using 1064-nm optical-dipole-trap lasers, *Phys. Rev. A* **84**, 043609 (2011).
- [37] J.-W. Chang, Y.-C. Huang, Z.-W. Xu, Y.-H. Kan, H.-H. Huang, J.-Z. Huang, K.-J. Fu, X.-D. Liu, and P.-C. Kuan, Multiphoton hyperfine raman transitions with different quantization axes, *Phys. Rev. A* **108**, 013308 (2023).
- [38] A. F. Bunkin and S. M. Pershin, Four photon low-frequency raman spectroscopy of single wall carbon nanotubes, *Laser Physics Letters* **4**, 656 (2007).
- [39] F. S. Cataliotti, R. Scheunemann, T. W. Hänsch, and M. Weitz, Superresolution of pulsed multiphoton raman transitions, *Phys. Rev. Lett.* **87**, 113601 (2001).
- [40] E. Brekke, J. O. Day, and T. G. Walker, Four-wave mixing in ultracold atoms using intermediate rydberg states, *Phys. Rev. A* **78**, 063830 (2008).
- [41] A. C. Lee, J. Smith, P. Richerme, B. Neyenhuis, P. W. Hess, J. Zhang, and C. Monroe, Engineering large stark shifts for control of individual clock state

- qubits, *Phys. Rev. A* **94**, 042308 (2016).
- [42] I. Jung, F. G. Schroer, and P. Richerme, Ion-based characterization of laser beam profiles for quantum information processing, *Entropy* **27**, 1115 (2025).
- [43] P. A. Barton, C. J. S. Donald, D. M. Lucas, D. A. Stevens, A. M. Steane, and D. N. Stacey, Measurement of the lifetime of the $3d^2D_{5/2}$ state in $^{40}\text{Ca}^+$, *Phys. Rev. A* **62**, 032503 (2000).
- [44] Z. Meir, M. Sinhal, M. S. Safronova, and S. Willitsch, Combining experiments and relativistic theory for establishing accurate radiative quantities in atoms: The lifetime of the $^2P_{3/2}$ state in $^{40}\text{Ca}^+$, *Phys. Rev. A* **101**, 012509 (2020).
- [45] G. Morigi, J. Eschner, and C. H. Keitel, Ground state laser cooling using electromagnetically induced transparency, *Phys. Rev. Lett.* **85**, 4458 (2000).
- [46] W. Nagourney, J. Sandberg, and H. Dehmelt, Shelved optical electron amplifier: Observation of quantum jumps, *Phys. Rev. Lett.* **56**, 2797 (1986).
- [47] A. S. Sotirova, J. D. Leppard, A. Vazquez-Brennan, S. M. Decoppet, F. Pokorny, M. Malinowski, and C. J. Ballance, High-fidelity heralded quantum state preparation and measurement (2024), arXiv:2409.05805.
- [48] T. Ruster, C. T. Schmiegelow, H. Kaufmann, C. Warschburger, F. Schmidt-Kaler, and U. G. Poschinger, A long-lived zeeman trapped-ion qubit, *Applied Physics B* **122**, 10.1007/s00340-016-6527-4 (2016).
- [49] A. R. et al, Helios: A 98-qubit trapped-ion quantum computer (2025), arXiv:2511.05465 [quant-ph].
- [50] G. J. Gregory, E. R. Ritchie, D. J. Wineland, D. T. C. Allcock, and J. O'Reilly, Sixth- and eighth-order ac stark shifts in a trapped calcium ion, In preparation (2026).
- [51] P. Barakhshan, A. Marrs, A. Bhosale, B. Arora, R. Eigenmann, and M. S. Safronova, extitPortal for High-Precision Atomic Data and Computation (version 2.0). University of Delaware, Newark, DE, USA. URL: <https://www.udel.edu/atom> [February 2022].
- [52] A. Kramida and Y. Ralchenko, NIST atomic spectra database, NIST standard reference database 78 (1999).
- [53] R. Han, H. K. Ng, and B.-G. Englert, Raman transitions without adiabatic elimination: a simple and accurate treatment, *Journal of Modern Optics* **60**, 255 (2013), <https://doi.org/10.1080/09500340.2013.770573>.
- [54] E. Hyyppä, A. Vepsäläinen, M. Papič, C. F. Chan, S. Inel, A. Landra, W. Liu, J. Luus, F. Marxer, C. Ockeloen-Korppi, S. Orbell, B. Tarasinski, and J. Heinsoo, Reducing leakage of single-qubit gates for superconducting quantum processors using analytical control pulse envelopes, *PRX Quantum* **5**, 030353 (2024).
- [55] I. D. Moore, W. C. Campbell, E. R. Hudson, M. J. Boguslawski, D. J. Wineland, and D. T. C. Allcock, Photon scattering errors during stimulated raman transitions in trapped-ion qubits, *Phys. Rev. A* **107**, 032413 (2023).
- [56] M. J. Boguslawski, Z. J. Wall, S. R. Vizvary, I. D. Moore, M. Bareian, D. T. C. Allcock, D. J. Wineland, E. R. Hudson, and W. C. Campbell, Raman scattering errors in stimulated-raman-induced logic gates in $^{133}\text{Ba}^+$, *Phys. Rev. Lett.* **131**, 063001 (2023).
- [57] I. Moore, A. Quinn, J. O'Reilly, J. Metzner, S. Brudney, G. Gregory, D. Wineland, and D. Allcock, Spontaneous raman scattering out of a metastable atomic qubit, *Physical Review A* **112**, 033106 (2025).
-

Appendix A: Beam geometry and level structure

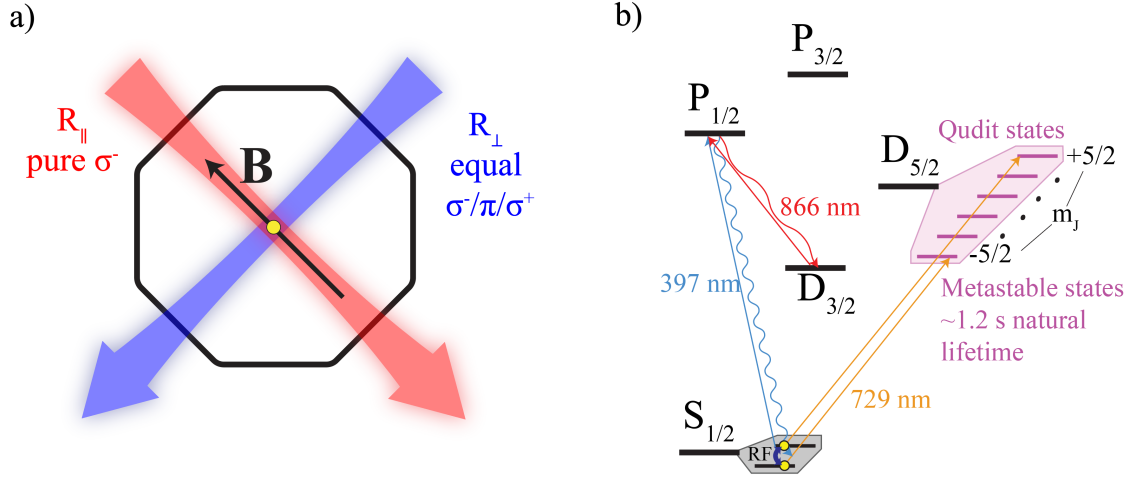


FIG. 5. **a)** Geometry of 976 nm Raman beams used to drive four- and six-photon transitions relative to quantization magnetic field direction. **b)** Relevant atomic structure of $^{40}\text{Ca}^+$ used in this work. 397 nm beam drives fluorescent $S_{1/2} \leftrightarrow P_{1/2}$ cycling transition with 866 nm beam to depump the $D_{3/2}$ manifold. 729 nm beam drives π pulses between S and m_J qudit states encoded in $D_{5/2}$ for state-preparation and readout of the qudit states. An optional RF π pulse between $S_{1/2}$ ground states is used to maximize the 729 transition Rabi frequency to each qudit state.

Appendix B: Four-photon Rabi frequency derivation

We present two methods to derive the Rabi frequencies of the higher order four- and six-photon transitions and provide example derivations for the exemplary four-photon transition in the main text. The first method follows the standard treatment of the two-photon Raman Rabi frequency derivation, wherein state amplitude equations of motions are generated via the Schrödinger equation, an adiabatic elimination approximation is taken to eliminate the virtual excited and intermediate states, and the equations of motion of the effective two-state system can be uncoupled. This method, however, can present ambiguities in the choice of frame to rotate to. Although not present in the example four-photon derivation given here, this does appear in the six-photon process we investigated. The second method employs time-dependent perturbation theory to calculate the leading order corrections to the time evolution of the state amplitudes and does not suffer the ambiguity sometimes present in the first method. Both methods arrive at the same result.

Differential equation approach

The coupling of states $|i\rangle$ and $|j\rangle$ via the k 'th beam with frequency ω_k is described by the ij 'th component of the Hamiltonian

$$V_{i,j} = -\frac{\hbar}{2}\Omega_{ij}e^{-i\omega_k t} \quad (\text{B1})$$

where Ω_{ij} is the complex single-beam Rabi frequency coupling the two states. In our treatment we include only terms of the laser-atom interaction Hamiltonian that correspond to the resonant dynamics, and we assume that off-resonant terms may be eliminated at the end of the calculation in a rotating wave approximation (RWA). We can then write out the full interaction Hamiltonian of the 7-level system shown in Fig. 1(a) in matrix form:

$$V(t) = -\frac{\hbar}{2} \begin{pmatrix} 0 & 0 & 0 & 0 & \Omega_{06}^* e^{i\omega_r t} & 0 & 0 \\ 0 & 0 & 0 & 0 & \Omega_{16}^* e^{i\omega_b t} & \Omega_{17}^* e^{i\omega_r t} & 0 \\ 0 & 0 & 0 & 0 & \Omega_{26}^* e^{i\omega_b t} & 0 & \Omega_{28}^* e^{i\omega_r t} \\ 0 & 0 & 0 & 0 & 0 & \Omega_{37}^* e^{i\omega_b t} & \Omega_{38}^* e^{i\omega_b t} \\ \Omega_{06} e^{-i\omega_r t} & \Omega_{16} e^{-i\omega_b t} & \Omega_{26} e^{-i\omega_b t} & 0 & 0 & 0 & 0 \\ 0 & \Omega_{17} e^{-i\omega_r t} & 0 & \Omega_{37} e^{-i\omega_b t} & 0 & 0 & 0 \\ 0 & 0 & \Omega_{28} e^{-i\omega_r t} & \Omega_{38} e^{-i\omega_b t} & 0 & 0 & 0 \end{pmatrix}. \quad (\text{B2})$$

where the state labels are defined in Fig. 1. By applying the Schrödinger equation with time evolution governed by Equation (B2), we generate the following set of coupled differential equations for the state amplitudes c_i :

$$\begin{aligned} \dot{c}_0 &= c_6 \frac{i\Omega_{06}^* e^{i\omega_r t}}{2} - \frac{iE_0}{\hbar} c_0 \\ \dot{c}_1 &= c_6 \frac{i\Omega_{16}^* e^{i\omega_b t}}{2} + c_7 \frac{i\Omega_{17}^* e^{i\omega_r t}}{2} - \frac{iE_1}{\hbar} c_1 \\ \dot{c}_2 &= c_6 \frac{i\Omega_{26}^* e^{i\omega_b t}}{2} + c_8 \frac{i\Omega_{28}^* e^{i\omega_r t}}{2} - \frac{iE_2}{\hbar} c_2 \\ \dot{c}_3 &= c_7 \frac{i\Omega_{37}^* e^{i\omega_b t}}{2} + c_8 \frac{i\Omega_{38}^* e^{i\omega_b t}}{2} - \frac{iE_3}{\hbar} c_3 \\ \dot{c}_6 &= c_0 \frac{i\Omega_{06} e^{-i\omega_r t}}{2} + c_1 \frac{i\Omega_{16} e^{-i\omega_b t}}{2} + c_2 \frac{i\Omega_{26} e^{-i\omega_b t}}{2} - \frac{iE_6}{\hbar} c_6 \\ \dot{c}_7 &= c_1 \frac{i\Omega_{17} e^{-i\omega_r t}}{2} + c_3 \frac{i\Omega_{37} e^{-i\omega_b t}}{2} - \frac{iE_7}{\hbar} c_7 \\ \dot{c}_8 &= c_2 \frac{i\Omega_{28} e^{-i\omega_r t}}{2} + c_3 \frac{i\Omega_{38} e^{-i\omega_b t}}{2} - \frac{iE_8}{\hbar} c_8. \end{aligned}$$

Anticipating a picture change, we rewrite the beam frequencies ω_r and ω_b in the coefficient for Ω_{ij} in terms of the state separation ω_{ij} and relevant beam detunings. For example, in the differential equation for \dot{c}_0 , we can replace ω_r with $\omega_{06} - \Delta_6$ and in the equation for \dot{c}_2 , we will replace ω_b with $\omega_{26} - \Delta_6 - \delta_2$. We can then re-write the coupled differential equations as

$$\begin{aligned}
\dot{c}_0 &= c_6 \frac{i\Omega_{06}^* e^{i(\omega_{06} - \Delta_6)t}}{2} - \frac{iE_0}{\hbar} c_0 \\
\dot{c}_1 &= c_6 \frac{i\Omega_{16}^* e^{i(\omega_{16} - \Delta_6 + \delta_1)t}}{2} + c_7 \frac{i\Omega_{17}^* e^{i(\omega_{17} - \Delta_7 + \delta_1)t}}{2} - \frac{iE_1}{\hbar} c_1 \\
\dot{c}_2 &= c_6 \frac{i\Omega_{26}^* e^{i(\omega_{26} - \Delta_6 - \delta_2)t}}{2} + c_8 \frac{i\Omega_{28}^* e^{i(\omega_{28} - \Delta_8 - \delta_2)t}}{2} - \frac{iE_2}{\hbar} c_2 \\
\dot{c}_3 &= c_7 \frac{i\Omega_{37}^* e^{i(\omega_{37} - \Delta_7)t}}{2} + c_8 \frac{i\Omega_{38}^* e^{i(\omega_{38} - \Delta_8)t}}{2} - \frac{iE_3}{\hbar} c_3 \\
\dot{c}_6 &= c_0 \frac{i\Omega_{06} e^{-i(\omega_{06} - \Delta_6)t}}{2} + c_1 \frac{i\Omega_{16} e^{-i(\omega_{16} - \Delta_6 + \delta_1)t}}{2} + c_2 \frac{i\Omega_{26} e^{-i(\omega_{26} - \Delta_6 - \delta_2)t}}{2} - \frac{iE_6}{\hbar} c_6 \\
\dot{c}_7 &= c_1 \frac{i\Omega_{17} e^{-i(\omega_{17} - \Delta_7 + \delta_1)t}}{2} + c_3 \frac{i\Omega_{37} e^{-i(\omega_{37} - \Delta_7)t}}{2} - \frac{iE_7}{\hbar} c_7 \\
\dot{c}_8 &= c_2 \frac{i\Omega_{28} e^{-i(\omega_{28} - \Delta_8 - \delta_2)t}}{2} + c_3 \frac{i\Omega_{38} e^{-i(\omega_{38} - \Delta_8)t}}{2} - \frac{iE_8}{\hbar} c_8
\end{aligned}$$

where we have defined δ_1 and δ_2 as the magnitude of the detunings $\omega - \omega_{01}$ and $\omega_{01} + \omega_{12} - \omega$, respectively, with ω defined as the detuning of the two beams $\omega_b - \omega_r$.

We now look to write the state amplitudes in a more illuminating representation. The mathematics simplifies if we transform the two primary amplitudes of interest (c_0 and c_3) to the interaction representation, $c'_i = c_i e^{\frac{iE_i t}{\hbar}}$. For the other states, we will transform to the field-interaction representation, the frame in which the state rotates at the detuning of the drive fields. The excited states in the $P_{3/2}$ will transform to $c''_i = c_i e^{i(\frac{E_i}{\hbar} - \Delta_i)t}$, and the intermediate states in the $D_{5/2}$ will transform to $c'_1 = c_1 e^{i(\frac{E_1}{\hbar} - \delta_1)t}$ and $c'_2 = c_2 e^{i(\frac{E_2}{\hbar} + \delta_2)t}$. The coupled equations of motion are then

$$\begin{aligned}
\dot{c}_0 &= c''_6 \frac{i\Omega_{06}^*}{2} \\
\dot{c}'_1 + i\delta_1 c'_1 &= c''_6 \frac{i\Omega_{16}^*}{2} + c''_7 \frac{i\Omega_{17}^*}{2} \\
\dot{c}'_2 - i\delta_2 c'_2 &= c''_6 \frac{i\Omega_{26}^*}{2} + c''_8 \frac{i\Omega_{28}^*}{2} \\
\dot{c}_3 &= c''_7 \frac{i\Omega_{37}^*}{2} + c''_8 \frac{i\Omega_{38}^*}{2} \\
\dot{c}'_6 + i\Delta_6 c'_6 &= c'_0 \frac{i\Omega_{06}}{2} + c'_1 \frac{i\Omega_{16}}{2} + c'_2 \frac{i\Omega_{26}}{2} \\
\dot{c}'_7 + i\Delta_7 c'_7 &= c'_1 \frac{i\Omega_{17}}{2} + c'_3 \frac{i\Omega_{37}}{2} \\
\dot{c}'_8 + i\Delta_8 c'_8 &= c'_2 \frac{i\Omega_{28}}{2} + c'_3 \frac{i\Omega_{38}}{2}.
\end{aligned}$$

We adiabatically eliminate [1] the $P_{3/2}$ states and intermediate states in the $D_{5/2}$ manifold by noting that the time derivatives in the equations for $i = 1, 2, 6, 7, 8$ are small compared to the $P_{3/2}$ state detunings Δ and the intermediate $D_{5/2}$ state detunings δ , so our equations of motion reduce to

$$\begin{aligned}
\dot{c}'_0 &= c''_6 \frac{i\Omega_{06}^*}{2} \\
c''_1 &\simeq \frac{1}{2\delta_1} (\Omega_{16}^* c''_6 + \Omega_{17}^* c''_7) \\
c''_2 &\simeq -\frac{1}{2\delta_2} (\Omega_{26}^* c''_6 + \Omega_{28}^* c''_8) \\
\dot{c}'_3 &= c''_7 \frac{i\Omega_{37}^*}{2} + c''_8 \frac{i\Omega_{38}^*}{2} \\
c''_6 &\simeq \frac{1}{2\Delta_6} (c'_0 \Omega_{06} + c''_1 \Omega_{16} + c''_2 \Omega_{26}) \\
c''_7 &\simeq \frac{1}{2\Delta_7} (c''_1 \Omega_{17} + c'_3 \Omega_{37}) \\
c''_8 &\simeq \frac{1}{2\Delta_8} (c''_2 \Omega_{28} + c'_3 \Omega_{38}).
\end{aligned}$$

Finally, we can uncouple the system of linear equations to reduce the problem to a single differential equation for amplitudes c'_0 and c'_3 of the form

$$\dot{c}'_0 = iC c'_0 + i \frac{\Omega_{03}^{(4)}}{2} c'_3 \quad (\text{B3})$$

where C is a term involving a.c. Stark shifts, and

$$\boxed{\Omega_{03}^{(4)} = \frac{\Omega_{06}^*}{8\Delta^2} \left(\frac{\Omega_{16}\Omega_{17}^*\Omega_{37}}{\delta_1} - \frac{\Omega_{26}\Omega_{28}^*\Omega_{38}}{\delta_2} \right)} \quad (\text{B4})$$

is the four-photon Rabi frequency. The derivation for the six-photon Rabi frequency follows analogously.

Time-dependent perturbation theory

In this section we present a derivation of Equation B4 via time dependent perturbation theory. We will work in the interaction representation. The Hamiltonian of the system is

$$H = H_0 + V(t) \quad (\text{B5})$$

where $V(t)$ is defined in Equation B2 and H_0 is the bare Hamiltonian of the ion. We first transform $V(t)$ into the interaction representation:

$$V_I(t) \equiv e^{iH_0 t/\hbar} V(t) e^{-iH_0 t/\hbar} \quad (\text{B6})$$

which, after substituting in $\delta_{0/1}$ as defined in the previous section, becomes

$$V_I(t) = \frac{\hbar}{2} \begin{pmatrix} 0 & 0 & 0 & 0 & \Omega_{06r} e^{-i\Delta t} & 0 & 0 \\ 0 & 0 & 0 & 0 & \Omega_{16b} e^{-i(\Delta-\delta_1)t} & \Omega_{17r} e^{-i(\Delta-\delta_1)t} & 0 \\ 0 & 0 & 0 & 0 & \Omega_{26b} e^{-i(\Delta+\delta_2)t} & 0 & \Omega_{28r} e^{-i(\Delta+\delta_2)t} \\ 0 & 0 & 0 & 0 & 0 & \Omega_{37b} e^{-i\Delta t} & \Omega_{38b} e^{-i\Delta t} \\ \Omega_{06r} e^{i\Delta t} & \Omega_{16b} e^{i(\Delta-\delta_1)t} & \Omega_{26b} e^{i(\Delta+\delta_2)t} & 0 & 0 & 0 & 0 \\ 0 & \Omega_{17r} e^{i(\Delta-\delta_1)t} & 0 & \Omega_{37b} e^{i\Delta t} & 0 & 0 & 0 \\ 0 & 0 & \Omega_{28r} e^{i(\Delta+\delta_2)t} & \Omega_{38b} e^{i\Delta t} & 0 & 0 & 0 \end{pmatrix}.$$

Now that we have the interaction Hamiltonian, we can solve for the time evolution propagator $U(t)$. If we initialize the state in $|0\rangle$ at time $t = 0$, $U(t)$ is defined as

$$|\psi(t)\rangle = U(t)|0\rangle \quad (\text{B7})$$

and the probability of the state being measured in state $|3\rangle$ after some time t is

$$P_{0 \rightarrow 3}(t) = |\langle 3|\psi(t)\rangle|^2 = |\langle 3|U(t)|0\rangle|^2. \quad (\text{B8})$$

To obtain an expression for the matrix element $\langle 3|U(t)|0\rangle$, we first expand $U(t)$ in a Dyson series:

$$U(t) = U^{(0)}(t) + U^{(1)}(t) + U^{(2)}(t) + U^{(3)}(t) + U^{(4)}(t) + \dots \quad (\text{B9})$$

with

$$\begin{aligned} U^{(0)}(t) &= 1 \\ U^{(1)}(t) &= \frac{-i}{\hbar} \int_0^t dt' V_I(t') \\ U^{(2)}(t) &= \left(\frac{-i}{\hbar}\right)^2 \int_0^t dt' \int_0^{t'} dt'' V_I(t') V_I(t'') \\ U^{(3)}(t) &= \left(\frac{-i}{\hbar}\right)^3 \int_0^t dt' \int_0^{t'} dt'' \int_0^{t''} dt''' V_I(t') V_I(t'') V_I(t''') \\ U^{(4)}(t) &= \left(\frac{-i}{\hbar}\right)^4 \int_0^t dt' \int_0^{t'} dt'' \int_0^{t''} dt''' \int_0^{t'''} dt'''' V_I(t') V_I(t'') V_I(t''') V_I(t'''') \\ &\vdots \end{aligned}$$

The matrix element $\langle 3|U^{(i)}(t)|0\rangle$ vanishes for all $i < 4$, a consequence of the angular momentum constraint of the dipole-coupled photons, and the leading correction to the propagator is therefore

$$\begin{aligned} \langle 3|U(t)|0\rangle &\approx \frac{\Omega_{06r} \Omega_{16b} \Omega_{17r} \Omega_{37b}}{16} \int_0^t dt' \int_0^{t'} dt'' \int_0^{t''} dt''' \int_0^{t'''} dt'''' e^{-it' \Delta + it'''' \Delta + it''(\Delta - \delta_1) - it''''(\Delta - \delta_1)} \\ &+ \frac{\Omega_{06r} \Omega_{26b} \Omega_{28r} \Omega_{38b}}{16} \int_0^t dt' \int_0^{t'} dt'' \int_0^{t''} dt''' \int_0^{t'''} dt'''' e^{-it' \Delta + it'''' \Delta + it''(\Delta + \delta_2) - it''''(\Delta + \delta_2)} \end{aligned}$$

Working through these integrals we find

$$\begin{aligned}
\langle 3|U(t)|0\rangle \approx & \frac{3\Omega_{06r}\Omega_{16b}\Omega_{17r}\Omega_{37b}}{16\Delta^2(\Delta-\delta_1)^2} - \frac{3e^{-it\Delta}\Omega_{06r}\Omega_{16b}\Omega_{17r}\Omega_{37b}}{16\Delta^2(\Delta-\delta_1)^2} - \frac{it\Omega_{06r}\Omega_{16b}\Omega_{17r}\Omega_{37b}}{8\Delta(\Delta-\delta_1)^2} \\
& - \frac{ie^{-it\Delta}t\Omega_{06r}\Omega_{16b}\Omega_{17r}\Omega_{37b}}{16\Delta(\Delta-\delta_1)^2} - \frac{\Omega_{06r}\Omega_{16b}\Omega_{17r}\Omega_{37b}}{16(\Delta-\delta_1)^2\delta_1^2} + \frac{e^{-it\delta_1}\Omega_{06r}\Omega_{16b}\Omega_{17r}\Omega_{37b}}{16(\Delta-\delta_1)^2\delta_1^2} \\
& + \frac{it\Omega_{06r}\Omega_{16b}\Omega_{17r}\Omega_{37b}}{16(\Delta-\delta_1)^2\delta_1} - \frac{\delta_1\Omega_{06r}\Omega_{16b}\Omega_{17r}\Omega_{37b}}{8\Delta^3(\Delta-\delta_1)^2} + \frac{e^{-it\Delta}\delta_1\Omega_{06r}\Omega_{16b}\Omega_{17r}\Omega_{37b}}{8\Delta^3(\Delta-\delta_1)^2} \\
& + \frac{it\delta_1\Omega_{06r}\Omega_{16b}\Omega_{17r}\Omega_{37b}}{16\Delta^2(\Delta-\delta_1)^2} + \frac{ie^{-it\Delta}t\delta_1\Omega_{06r}\Omega_{16b}\Omega_{17r}\Omega_{37b}}{16\Delta^2(\Delta-\delta_1)^2} \\
& + \frac{3\Omega_{06r}\Omega_{26b}\Omega_{28r}\Omega_{38b}}{16\Delta^2(\Delta+\delta_2)^2} - \frac{3e^{-it\Delta}\Omega_{06r}\Omega_{26b}\Omega_{28r}\Omega_{38b}}{16\Delta^2(\Delta+\delta_2)^2} - \frac{it\Omega_{06r}\Omega_{26b}\Omega_{28r}\Omega_{38b}}{8\Delta(\Delta+\delta_2)^2} \\
& - \frac{ie^{-it\Delta}t\Omega_{06r}\Omega_{26b}\Omega_{28r}\Omega_{38b}}{16\Delta(\Delta+\delta_2)^2} - \frac{\Omega_{06r}\Omega_{26b}\Omega_{28r}\Omega_{38b}}{16\delta_2^2(\Delta+\delta_2)^2} + \frac{e^{-it\Delta+it(\Delta+\delta_2)}\Omega_{06r}\Omega_{26b}\Omega_{28r}\Omega_{38b}}{16\delta_2^2(\Delta+\delta_2)^2} \\
& - \frac{it\Omega_{06r}\Omega_{26b}\Omega_{28r}\Omega_{38b}}{16\delta_2(\Delta+\delta_2)^2} + \frac{\delta_2\Omega_{06r}\Omega_{26b}\Omega_{28r}\Omega_{38b}}{8\Delta^3(\Delta+\delta_2)^2} - \frac{e^{-it\Delta}\delta_2\Omega_{06r}\Omega_{26b}\Omega_{28r}\Omega_{38b}}{8\Delta^3(\Delta+\delta_2)^2} \\
& - \frac{it\delta_2\Omega_{06r}\Omega_{26b}\Omega_{28r}\Omega_{38b}}{16\Delta^2(\Delta+\delta_2)^2} - \frac{ie^{-it\Delta}t\delta_2\Omega_{06r}\Omega_{26b}\Omega_{28r}\Omega_{38b}}{16\Delta^2(\Delta+\delta_2)^2}
\end{aligned}$$

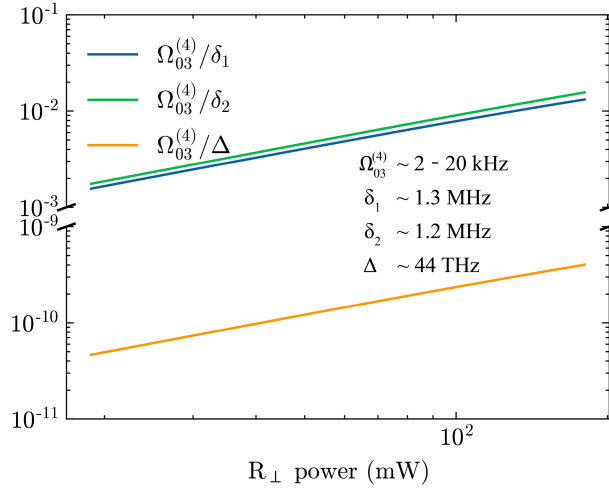


FIG. 6. Ratio of four-photon Rabi frequency (analytic) to detuning from P and intermediate D states. Adiabatic elimination approximation for such states (and corresponding terms in $\langle 3|U(t)|0\rangle$) is valid in the regime that the curve is $\ll 1$. Colored terms in the expression for $\langle 3|U(t)|0\rangle$ are approximated to be zero, justified by corresponding colored curve in the figure.

At this point we will make some approximations to simplify the expression. In our system the P state detuning is much greater than the detuning from the intermediate states: $\Delta \gg \delta$. In addition, we must still make an approximation analogous to the adiabatic elimination approximation: the Rabi frequency of the transition is much slower than the detuning from the states that off-resonantly facilitate the transition (P states and intermediate states in $D_{5/2}$). The orange terms above are approximately zero in the regime where $\Omega_{03}^{(4)}/\Delta \ll 1$, and the blue and green terms can be approximated as zero in the regime where $\Omega_{03}^{(4)}/\delta_{1/2} \ll 1$.

Thus, we have

$$\langle 3|U(t)|0\rangle \approx \frac{\Omega_{06}^* t}{16\Delta^2} \left(\frac{\Omega_{16}\Omega_{17}^*\Omega_{37}}{\delta_1} - \frac{\Omega_{26}\Omega_{28}^*\Omega_{38}}{\delta_2} \right) \quad (\text{B10})$$

and we can make the definition

$$\boxed{\Omega_{03}^{(4)} \equiv \frac{\Omega_{06}^*}{8\Delta^2} \left(\frac{\Omega_{16}\Omega_{17}^*\Omega_{37}}{\delta_1} - \frac{\Omega_{26}\Omega_{28}^*\Omega_{38}}{\delta_2} \right)}. \quad (\text{B11})$$

The probability to transfer population from $|0\rangle$ to $|3\rangle$ for short times t is

$$P_{0\rightarrow 3}(t) = |\langle 3|U(t)|0\rangle|^2 \approx \frac{|\Omega_{03}^{(4)} t|^2}{4}. \quad (\text{B12})$$

To show that we have obtained the four-photon Rabi frequency, we take note of the Taylor expansion

$$\sin^2\left(\frac{x}{2}\right) = \frac{x^2}{4} - \frac{x^4}{48} + \dots \quad (\text{B13})$$

and we posit that higher orders of perturbation theory will generate the higher order terms in the Taylor expansion for $\sin^2\frac{x}{2}$. This implies that the probability to measure the state in $|3\rangle$ after preparing in $|0\rangle$ and driving for a time t evolves as

$$P_{0\rightarrow 3}(t) = \sin^2\left(\frac{\Omega_{03}^{(4)} t}{2}\right) \quad (\text{B14})$$

with $\Omega_{03}^{(4)}$ the same four-photon Rabi frequency we calculated in the previous section.

Appendix C: Numerical simulations

We seek to validate the adiabatic elimination of the intermediate $D_{5/2}$ states, which is the new, non-standard approximation made in this work. To this end, we numerically simulate the dynamics under a Hamiltonian considering couplings between states within $D_{5/2}$ and $P_{3/2}$. We reduce the problem to a six-level system by adiabatically eliminating the P states but not the D states. In this Hamiltonian we do not drop any fast rotating terms, as we did in Equation (B2), and include all possible beam couplings.

We see a direct breakdown in the approximation at high beam powers, resulting in fast, small-amplitude dynamics on top of the main Rabi flopping envelope and non-negligible population of intermediate states (see Fig. 13). In Fig. 7, we plot the ratio of the four-photon Rabi frequency as predicted by our numerical simulations to the result of Equation (3) as a function of the analytic four-photon π -time, which is a function of the power in the R_{\perp} beam. We see that the predicted Rabi frequencies converge at low beam powers, suggesting that adiabatic elimination of the intermediate $D_{5/2}$ levels is valid in this regime (see Fig 6).

Appendix D: Modeling of Spin Decoherence

To model spin decoherence we consider the effects of both slow and fast ambient magnetic field fluctuations. We model fast frequency noise as a simple exponential damping of the Rabi oscillation amplitude in time parameterized by damping rate γ . We model decoherence induced by low frequency noise as a shot-to-shot static qubit frequency offset δ drawn from a normal distribution with a width in frequency space fixed from a fit to experimental Ramsey time-series data $\sigma_f^{(i)} = 1/\sigma_t^{(i)}$.

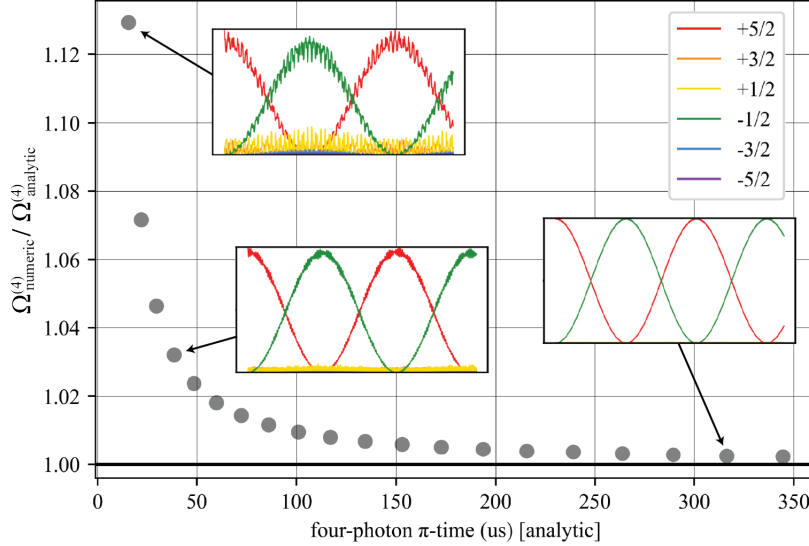


FIG. 7. Analytically predicted four-photon Rabi frequency divided by the numerically simulated Rabi frequency at various driving strengths. As the transition π -time increases (decreasing beam power) the two results converge, justifying the $D_{5/2}$ adiabatic elimination approximation. Inset figures are numerically-simulated resonant dynamics.

We probed the coherence between states $m_J = +5/2$ and $m_J = +3/2$ by measuring the decay in Ramsey contrast (without a spin echo) as a function of delay time (see Fig. 8) using rf qubit manipulations, and expect the loss in Ramsey contrast to be dominated by the low frequency noise. The Ramsey contrast (black circles) fits well to a Gaussian decay function (solid black) with a fit standard deviation of $\sigma_t^{(1)} = 0.61(8)$ ms corresponding to a $1/e$ coherence time $\tau^{(1)} = \sqrt{2}\sigma_t^{(1)} = 0.87(12)$ ms. Numerical simulations (black \times markers) assuming the corresponding $\sigma_f^{(1)} = 1.6(2)$ kHz agree well with both the experimental data and analytic Gaussian decay function. As the presented four- and six-photon transitions cover $\Delta m_J = 3$ and 4, respectively, we assume $\sigma_t^{(3)} = \sigma_t^{(1)}/3$ (solid blue) and $\sigma_t^{(4)} = \sigma_t^{(1)}/4$ (solid red).

Because off-resonant Rabi oscillations have a closed analytic expression, we can write the functional form of Rabi oscillations in our model as a weighted average of detuned Rabi oscillations where Ω is the Rabi frequency and γ is the heuristic damping constant to account for loss in contrast due to faster noise components not seen in the slow noise dominated Ramsey data:

$$P(t, \Omega, \sigma_f, \gamma) = \frac{1}{\sigma\sqrt{2\pi}} \sum_{\delta} \frac{\Omega}{\sqrt{\Omega^2 + \delta^2}} \sin^2 \frac{t\sqrt{\Omega^2 + \delta^2}}{2} e^{-\frac{\sigma^2}{2\delta^2} - \gamma t}. \quad (\text{D1})$$

For each data set, we fit Ω and γ in Equation (D1) while holding σ_f fixed. Shown in Fig. 9 are the fits to the damping term γ for each data set, with example Rabi oscillations in the insets. The Ω results are presented in Fig. 2b in the main text.

Appendix E: Beam polarization and intensity calibration

The analytic expressions for the presented four- and six-photon transition Rabi frequencies (Equations (3) and (4)) rely on precise calibration of the intensity of each polarization component of the R_{\perp} and R_{\parallel} beams. To carry out this calibration, we performed a series of auxiliary experiments and fit intensities to the experimental data. At the end of this section we present a table summarizing the constrained parameters for the two beams.

R_{\perp} polarization constraint

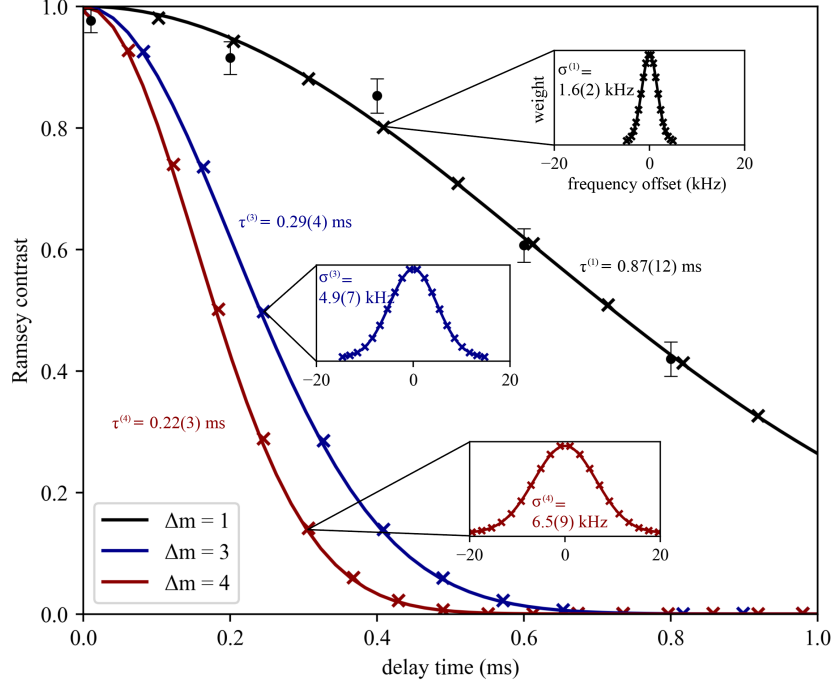


FIG. 8. Ramsey contrast as a function of delay time between two $\pi/2$ pulses on the $m_J = +5/2 \leftrightarrow +3/2$ transition (black circles) with a Gaussian function fit to data (black line). Blue and red lines are projected contrast decay on $+5/2 \leftrightarrow -1/2$ and $+5/2 \leftrightarrow -3/2$ transitions, respectively. \times marks are results of numerically simulated Ramsey sequences under a normally distributed shot-to-shot static qubit frequency offset with distributions shown in the insets.

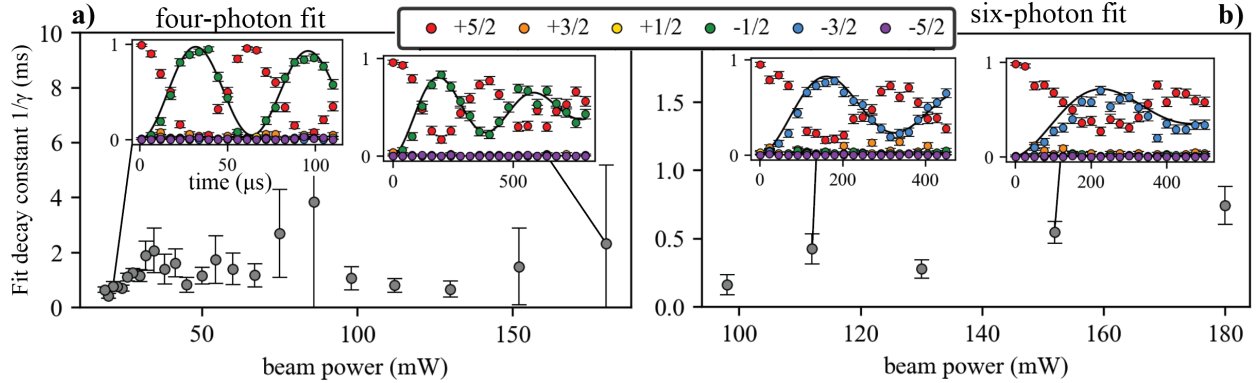


FIG. 9. Returned fit parameter γ for each set of resonant Rabi-oscillations for four (a) and six (b) photon driven time dynamics.

Nominally, the R_{\perp} beam has equal components of $\sigma^{-}/\pi/\sigma^{+}$ polarizations to null the lowest (second) order differential a.c. Stark shifts throughout the $D_{5/2}$ manifold. We assume the beam propagates perpendicular to the quantization axis and thus has equal power in the σ^{-} and σ^{+} polarization components. We estimate the π component by measuring the differential a.c. Stark shift imparted on the $m_J = +5/2 \leftrightarrow +3/2$ transition by 180 mW of the R_{\perp} beam. We measure the unperturbed Zeeman and R_{\perp} shifted splittings via rf Rabi spectroscopy to be 2.6338(3) and 2.6339(3) MHz, respectively, corresponding to a differential shift of 0.1(4) kHz. To obtain an estimate for the bound on the beams polarization makeup we calculate the differential a.c. Stark shift on the transition as a function of relative beam power in π and σ^{+} polarization up to 8th order in perturbation theory [50] assuming a 30 μm beam waist (see Figure 10),

and compare to the value we measure experimentally.

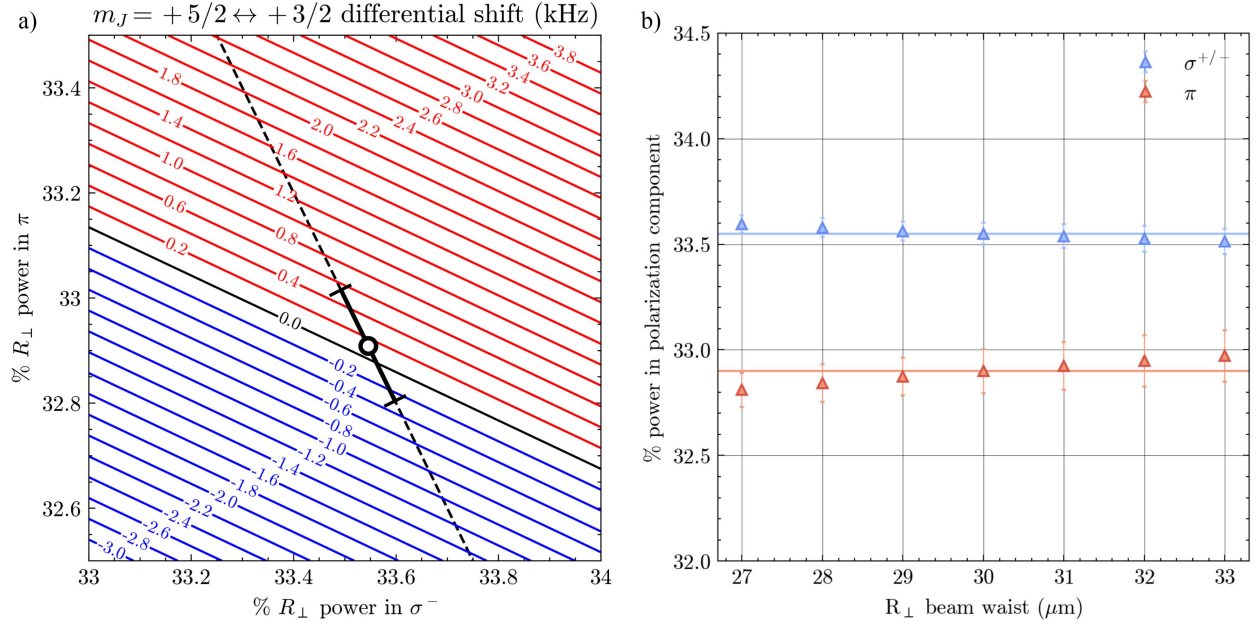


FIG. 10. **a)** Differential a.c. Stark shift (kHz) up to eighth order in perturbation on the $m_J = +5/2 \leftrightarrow +3/2$ qubit with R_{\perp} beam illuminating the ion at 180 mW, assuming at 30 μm beam waist. Dashed line represents the constraint that $\sigma^{-/+}$ polarizations have the same relative intensities. **b)** Constrained R_{\perp} beam polarization components as a function of reasonable beam waists in the experiment.

We constrain the polarization breakdown of the R_{\perp} beam to be 33.55(5)% $\sigma^{+/-}$ and 32.9(1)% π (see Figure 10a) based on the experimentally measured differential shift. We also find polarization breakdowns that agree within error over a large range of beam waist sizes relative to the experiment Figure 10(b).

R_{\parallel} polarization and beam waist constraints

Nominally, the R_{\parallel} beam is purely σ^{-} polarized. To estimate the impurity in the polarization of the beam we measured the frequency splittings between nearest-neighbor states in the $D_{5/2}$ manifold under increasing R_{\parallel} beam powers. To determine the splitting frequency between states $|i\rangle$ and $|i+1\rangle$ we prepare the ion in the $|i\rangle$ state and perform Rabi spectroscopy by driving with RF and measuring population in the $|i+1\rangle$ state while scanning the RF frequency. Shown in Fig. 11b are the measured nearest neighbor splittings in $D_{5/2}$ at increasing R_{\parallel} beam power. We can then write out analytic expressions for the splittings considering ac Stark shifts induced by the R_{\parallel} beam coupling to $F_{7/2}$ and $P_{3/2}$ states up to and including second and eighth order in perturbation, respectively, [50] parameterized by the intensity in each polarization component. The three free parameters of the R_{\parallel} beam are under constrained by the splittings alone, and we additionally measure the Raman Rabi frequency of the $m_J = +5/2 \leftrightarrow +3/2$ transition at the two-photon resonance condition and with increasing R_{\perp} beam powers while the R_{\parallel} beam power held constant at 195 mW, and perform a joint fit of the two data sets to fully constrain the beam properties.

Initially, we sought to fit the analytic expression of the well-known two-photon Rabi frequency to the data but found that the experimental measurements of the Rabi frequency did not follow the expected $\sqrt{P_{\perp}}$ scaling within error. We attribute this discrepancy to higher order resonant four-photon processes driving the transition simultaneously, with expected four-photon pathways contributing on the $\sim 10\%$ level. We numerically simulate the transition (blue curve in Fig 10a) and find matching scaling of the simulated and experimentally obtained Rabi frequency with R_{\perp} power, suggesting that the higher order processes are captured by the simulation.

We performed a joint least-squares fit of the data shown in Fig 11ab, floating the beam waists (w_0) of the R_{\perp} and R_{\parallel} beams and the amplitudes of the polarization vector for the R_{\parallel} beam with $\mathbf{E} =$

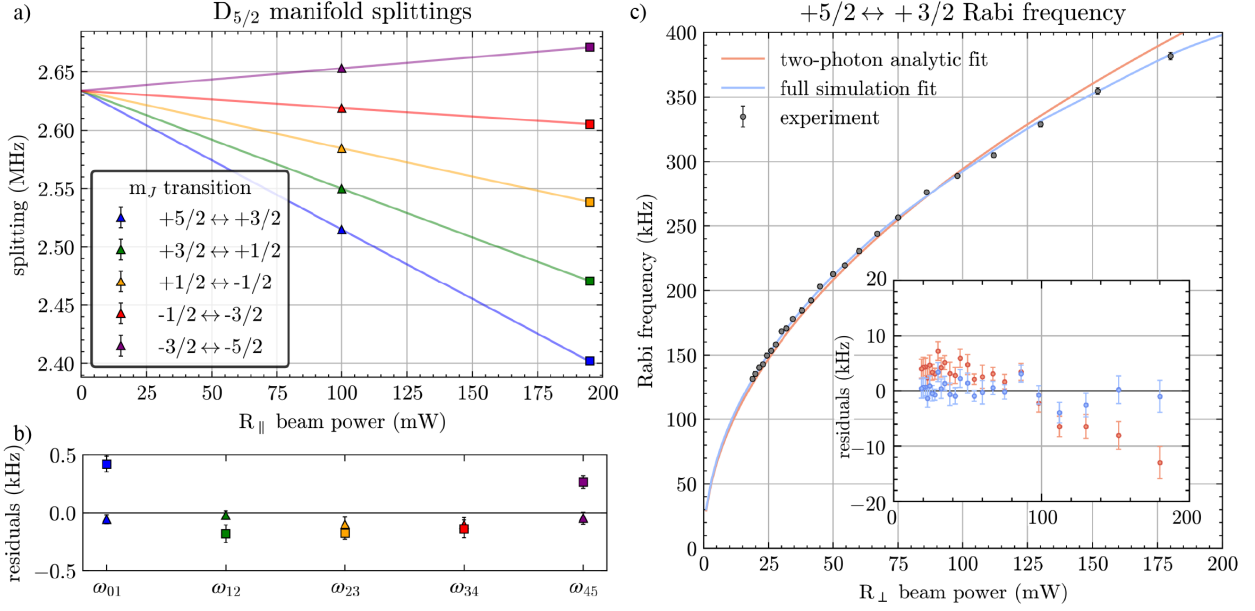


FIG. 11. **a)** Rabi frequency of the $m_J = +5/2 \leftrightarrow +3/2$ transition as a function of power in the R_{\perp} beam, with the power in R_{\parallel} held fixed at 195 mW. Red curve is a fit to the analytic two-photon Rabi frequency expression. Blue curve is a fit to a full numerical simulation of the system natively including higher order resonant four-photon corrections to the Rabi frequency, with residuals shown in inset. **b)** Experimentally measured nearest-neighbor state splittings within the $D_{5/2}$ manifold at various R_{\parallel} beam powers. Solid curves are fits to analytic expressions for the differential shift up to and including eighth order corrections. **c)** Residuals to fit at 100 mW in R_{\parallel} .

TABLE I. Summary of fit beam waist and polarization components of the Raman beams used for theoretical four- and six-photon analytic Rabi frequencies (see Fig. 2b.)

Parameter	R_{\parallel} beam				R_{\perp} beam			
	w_0 (μm)	$e_{\sigma-}^2$	e_{π}^2	$e_{\sigma+}^2$	w_0 (μm)	$e_{\sigma-}^2$	e_{π}^2	$e_{\sigma+}^2$
Fit value	30.60(9)	87.2(3)%	0.0(3)%	12.8(1)%	32.16(23)	33.55(5)%	32.9(1)%	33.55(5)

$|E\rangle(\mathbf{e}_{\sigma-} + \mathbf{e}_{\pi} + \mathbf{e}_{\sigma+})$. Together with the constraints on the R_{π} beam polarization (Fig 10, this parameterization fully describes the R_{\perp} and R_{\parallel} beams. We present the fit parameters in Table I.

Appendix F: F state coupling

The 976 nm beams we use are -44 THz red-detuned from the 854 nm $D_{5/2} \leftrightarrow P_{3/2}$ transition. The beams are also $-1,322$ THz red-detuned from the 184 nm $D_{5/2} \leftrightarrow F_{7/2}$ and $D_{5/2} \leftrightarrow F_{5/2}$ transitions [51, 52]. In this section, we discuss small corrections to Equations (3) and (4) considering couplings to the F manifolds. The matrix elements coupling manifolds $3D_{5/2} \leftrightarrow 4P_{3/2}$, $3D_{5/2} \leftrightarrow 4F_{5/2}$, and $3D_{5/2} \leftrightarrow 4F_{7/2}$ are (in atomic units) $3.283(6)$, $0.5164(56)$, and $2.309(25)$ respectively, and we ignore couplings to $F_{5/2}$ due to the relatively small matrix element.

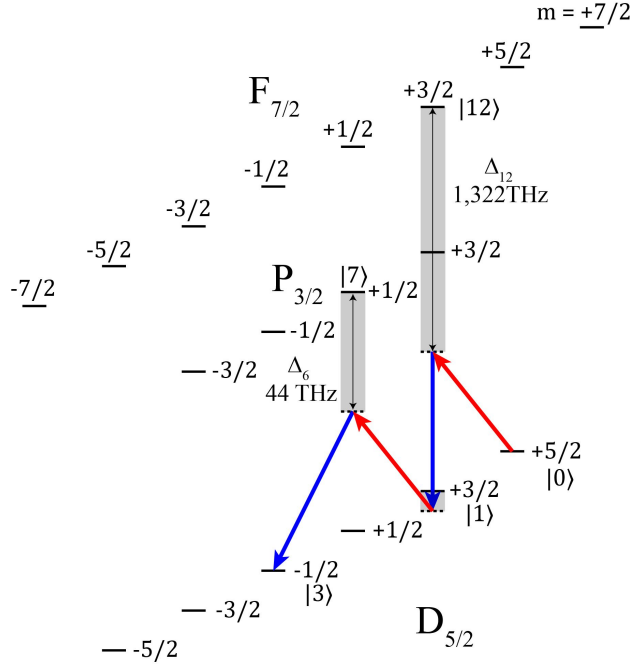


FIG. 12. Example resonant four-photon pathway from $m_J = +5/2$ to $m_J = -1/2$ in $D_{5/2}$ with couplings to excited states $F_{7/2}, m_J = +3/2$ and $P_{3/2}, m_J = +1/2$. The corresponding contribution to the four-photon Rabi frequency is given in Equation (F1). Other resonant pathways are not illustrated.

There are many pathways involving these manifolds that facilitate the $+5/2 \leftrightarrow -1/2$ four-photon transition. We neglect terms where the F states are coupled to more than once in a given pathway, as the corresponding term for the Rabi frequency contains the larger Δ_F squared (or cubed) in the denominator. Pathways coupling to both the F and P states, however, contribute percent-level effects. In Fig. 12 we show an example pathway for the four-photon transition we present in the main text including coupling to the $F_{7/2}$ manifold. This pathway adds the term

$$\frac{\Omega_{012}^* \Omega_{112} \Omega_{17}^* \Omega_{37}}{8 \Delta_{12} \Delta_7 (\omega_r - \omega_{01})} \quad (\text{F1})$$

to the four-photon Rabi frequency (Equation (3)). Corresponding terms for all relevant pathways for both the four- and six-photon transitions are included in the analytic results presented in Fig. 2.

Appendix G: Intermediate state population

Numerical simulations of the four- and six-photon dynamics also provide insight into the time evolution of the intermediate state amplitudes, which are assumed to be zero in the analytic treatment. As can be seen in Fig. 7, the population of the intermediate states oscillate much faster than the resonant transition Rabi frequency. We choose to place the maximum population of intermediate states during resonant dynamics as

a conservative lower bound on the transfer infidelity. Shown in Fig. 13 are the maximum intermediate state populations measured in the four-photon $+5/2 \leftrightarrow -1/2$ resonant time dynamics at different beam powers. We also plot the numerically predicted bounds on the intermediate state populations resultant from the simulations (solid lines).

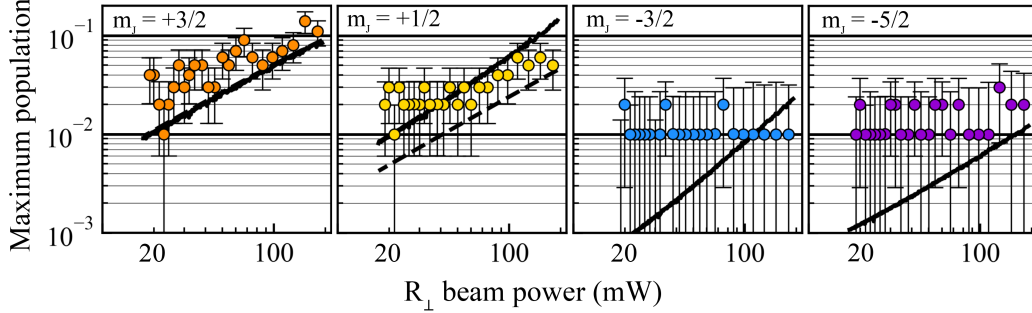


FIG. 13. Maximum intermediate state population during resonant $m = +5/2 \leftrightarrow -1/2$ four-photon time dynamics at different R_{\perp} beam powers. Solid curves are predictions from numerical simulation while dashed curves correspond to analytic ansatzes (Equations (G2) and G3).

The $m_J = -3/2$ and $-5/2$ population bounds do not increase with beam power and remain around the measured qudit SPAM error. On the other hand, the bounds for the $+3/2$ and $+1/2$ states do increase with beam power in agreement with our numerical simulations. Additionally, we posit analytic expressions for the intermediate state populations as a generalization of previous work setting a bound on intermediate state population for a three-level cascade system [53].

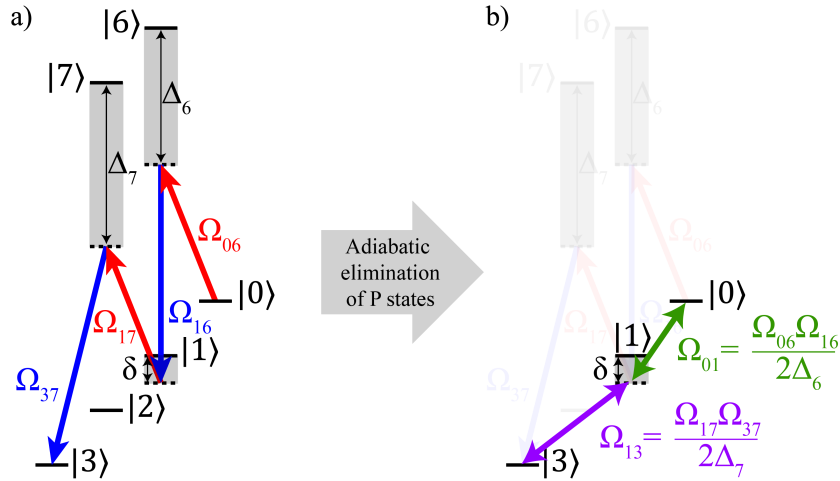


FIG. 14. a). Diagram of a single resonant pathway driving a four-photon transition between angular momentum state $m_J = +5/2$ and $-1/2$. b). Mapping of the 5 state system with P state couplings to a three level cascade system, with P states adiabatically eliminated.

Shown in Fig. 14a is a single resonant pathway for the four-photon transition presented in the main text. Upon adiabatic elimination of the P states the five-state system is effectively simplified to a three-state cascade system for which analytic expressions for the bound on intermediate state population $|P_1|$ during resonant dynamics has been worked out in Ref. [53]:

$$|P_1| = \frac{|\Omega_{01}^2|}{|\Omega_{01}^2| + |\Omega_{13}^2| + \delta^2}. \quad (\text{G1})$$

We can estimate bounds on the population of intermediate states $m_J = +3/2$ and $+1/2$ during the resonant four-photon process (Fig. 1) by replacing the single beam Rabi frequencies in Equation (G1) with

the corresponding two-beam Raman Rabi frequencies considering couplings to the P states. Assuming maximum populations of the intermediate states is small, the bounds for states $m_J = +3/2$ and $+1/2$ are

$$|P_{+3/2}| = \frac{\Omega_{06}^2 \Omega_{16}^2}{\Omega_{06}^2 \Omega_{16}^2 + \Omega_{17}^2 \Omega_{37}^2 + 4\Delta^2 (\omega_r - \omega_{01})^2} \quad (\text{G2})$$

$$|P_{+1/2}| = \frac{\Omega_{06}^2 \Omega_{26}^2}{\Omega_{06}^2 \Omega_{26}^2 + \Omega_{28}^2 \Omega_{38}^2 + 4\Delta^2 (\omega_{01} + \omega_{12} - \omega_r)^2}. \quad (\text{G3})$$

We plot Equations (G2) and (G3) as dashed lines in Fig. 13 and find reasonable agreement between the analytic predictions and numerical simulations.

Appendix H: Extension to high fidelity

In this section we discuss pathways towards higher fidelity control of the four-photon transition discussed in the main text, including considerations of the dominant error sources: population of intermediate states as a breakdown of the adiabatic elimination approximation, decoherence of the qudit spin states caused by ambient magnetic field fluctuations, and errors incurred through spontaneous Raman scattering. We do not discuss the six-photon transition in detail, but similar arguments can be made to increase its fidelity as well.

Intermediate state population

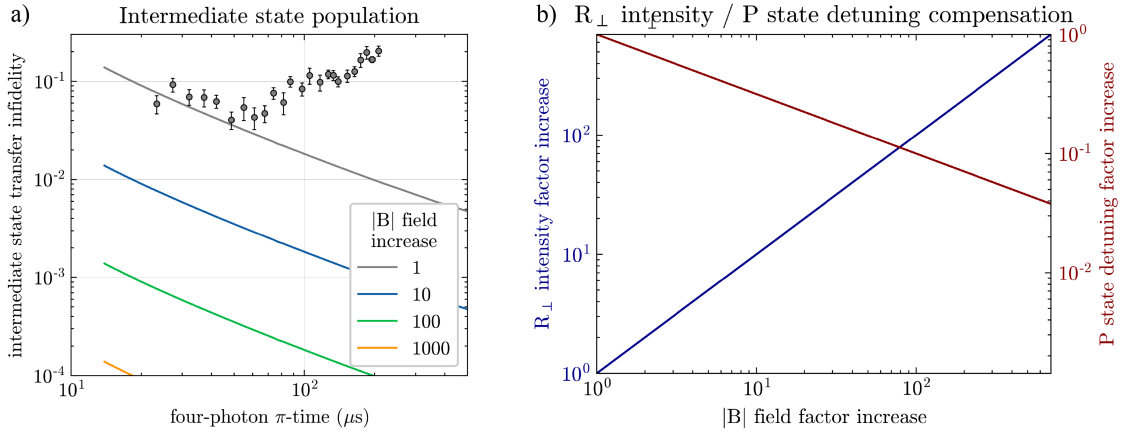


FIG. 15. **a)** Four-photon π pulse transfer infidelity manifested as population of intermediate states, determined by numerical simulations (black), and extrapolated to other Zeeman splittings according to analytic model (Equation G2). **b)** Compensation factors of R_{\perp} intensity or P state detuning to maintain constant four-photon Rabi frequency for different Zeeman splitting increases.

One strategy to reduce intermediate state population is increasing the magnitude of the quantization magnetic field, thus increasing δ_1 and δ_2 (see Figure 6). In principle, this strategy can reduce the associated infidelity arbitrarily. However, the reduction in Rabi frequency when increasing δ_1 and δ_2 must be accounted for with a corresponding increase in beam intensity or decrease in P state detuning, and we find that lowering the intermediate state population to $< 10^{-4}$ level requires a 10^3 factor increase in quantization field strength and beam intensity. Greater beam intensity for the same pulse length causes significantly more Raman scattering errors, making them the dominant error at 100s of Gauss.

Alternatively, we can view the population of intermediate states as a consequence of off-resonant Rabi oscillations. For a square pulse, the power spectral density (PSD) takes on a $\text{sinc}^2(f)$ profile, with lobes that fall off as $1/f$ away from the carrier frequency. We consider applying an amplitude envelope to the R_{\perp} beam

to lower the PSD at the intermediate state locations in frequency space and reduce the population driven to the intermediate states [54]. We consider \sin^2 and \sin^4 amplitude ramps on the R_\perp beam (while keeping the shape of the R_\parallel beam pulse square) and carry out numerical simulations of the dynamics to estimate the improvement of four-photon π pulse transfer fidelity. We maintain the same peak power as the square pulses and use ramp parameters such that the total pulse time is increased by a factor of $1.25\times$.

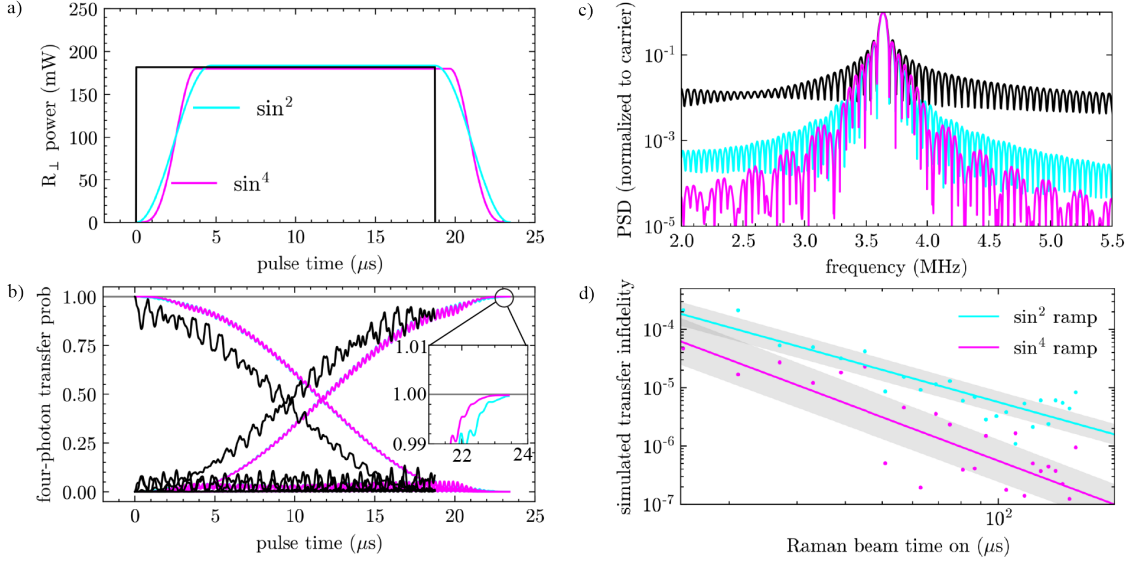


FIG. 16. **a)** Amplitude envelopes for the R_\perp beam. **b)** Simulated population dynamics for the four-photon transition π pulse driven by the pulse shaping shown in a). **c)** PSD of the three pulses driving population in b) with envelopes shown in a). **d)** Simulated π pulse transfer infidelity with the pulse shaping shown in a) at different π times, corresponding to different R_\perp peak beam powers.

Illustrated in Figure 16a are the three amplitude envelopes we consider, with the peak power in R_\perp and R_\parallel beams set to 180 and 195 mW, respectively, coinciding with the maximum powers used in the experiment. In Figure 16b we show the simulated population dynamics of the full six-level system corresponding to a π pulse with pulse shaping illustrated in Figure 16a, with the amplitude of intermediate state population oscillations clearly diminished due to the pulse shaping, especially at the beginning and end of the pulse. The corresponding PSD of each pulse is shown in Figure 16c, illustrating the several orders of magnitude reduction in PSD at the intermediate state locations relative to the carrier. Finally, we simulate π pulses with pulse shaping at different powers of the R_\perp beam, corresponding to different π times. We take the final population in $|3\rangle$ after simulating a π pulse on the system initialized in $|0\rangle$ as the transfer fidelity, and fit a straight line to the logarithms of the simulated infidelity vs π time data shown in Figure 16d.

Any un-nulled differential a.c. Stark shifts between the states $|0\rangle$ and $|3\rangle$ cause the four-photon transition to shift out of resonance during amplitude ramping, leading to a small transfer infidelity. a.c. Stark shifts up to 8th order in perturbation theory contribute kHz size differential shifts to the four-photon resonance at these beam powers [cite 'in prep.' paper]. In the simulations mentioned above we adjust the R_\perp beam polarization according to Figure 17 to null the differential shift as effectively as possible.

Spin decoherence

We point to a demonstration of long Zeeman qubit spin coherence in the $S_{1/2}$ manifold of a single trapped and laser cooled $^{40}\text{Ca}^+$ ion [48] as an example of achievable performance in state-of-the-art systems with $\text{Sm}_2\text{Co}_{17}$ permanent magnets supplying a 0.37 mT quantizing magnetic field at the ion and a two-layer μ -metal shield to protect against ambient magnetic field fluctuations. Shown in Fig. 18 is the Ramsey contrast as a function of delay time carried out in our experimental setup (black circles) and in the state-of-the-art setup [48] (orange). The ratio of sensitivities to magnetic field fluctuations between the ground state qubit and a $\Delta m = 1$ qubit encoded in the $D_{5/2}$ manifold is given by the ratio of Landé g factors of the two manifolds. Accordingly, a $\Delta m = 1$ qubit in the $D_{5/2}$ manifold has $3/5\times$ the magnetic field sensitivity

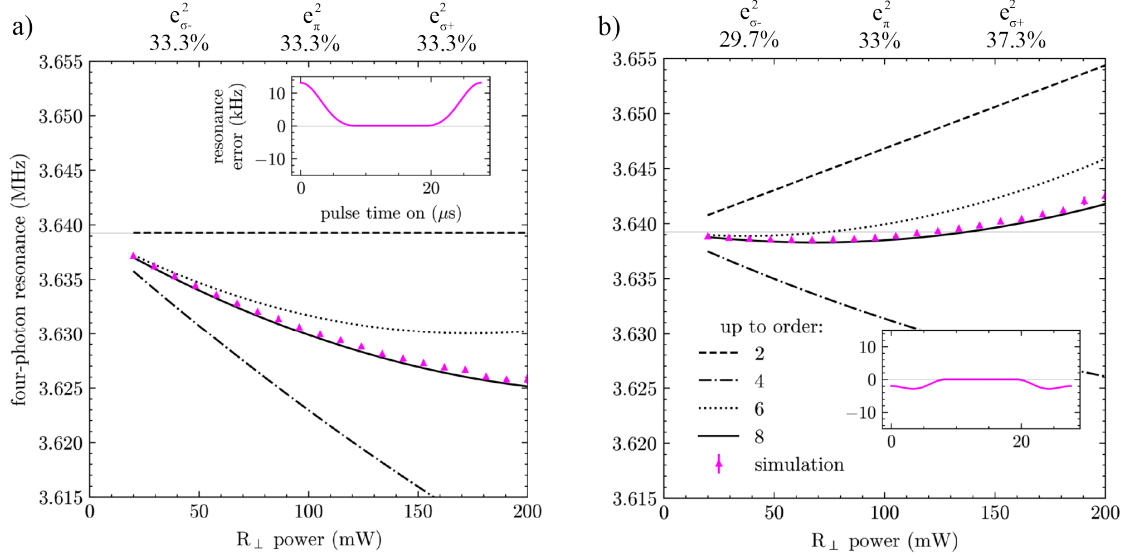


FIG. 17. **a)** Simulated four-photon resonance with equal powers in each polarization component of the R_{\perp} beam. Black curves correspond to analytic corrections from perturbation theory up to second (dashed), fourth (dot-dashed), sixth (dotted) and eighth (solid) order [50]. Inset shows time-dependent shift during the π pulse with \sin^2 amplitude ramps on the R_{\perp} beam and maximum beam powers. **b)** Same as a) with R_{\perp} polarizations chosen to reduce time-dependent shift.

to that of the ground qubit, corresponding to an expected $1/e$ coherence time of 850 ms. We account for the increased magnetic field sensitivity of the higher Δm transitions within $D_{5/2}$ as we do in Appendix D and model decoherence in the same way, with the widths of shot-to-shot qubit errors extrapolated from the predicted coherence time. We expect an improvement of the $\Delta m = 3$ four-photon transition coherence time of $\times 966$ in the apparatus used in Ref. [48]. Similarly, we adjust the damping constant by that same factor to find $1/\gamma = 578$ ms.

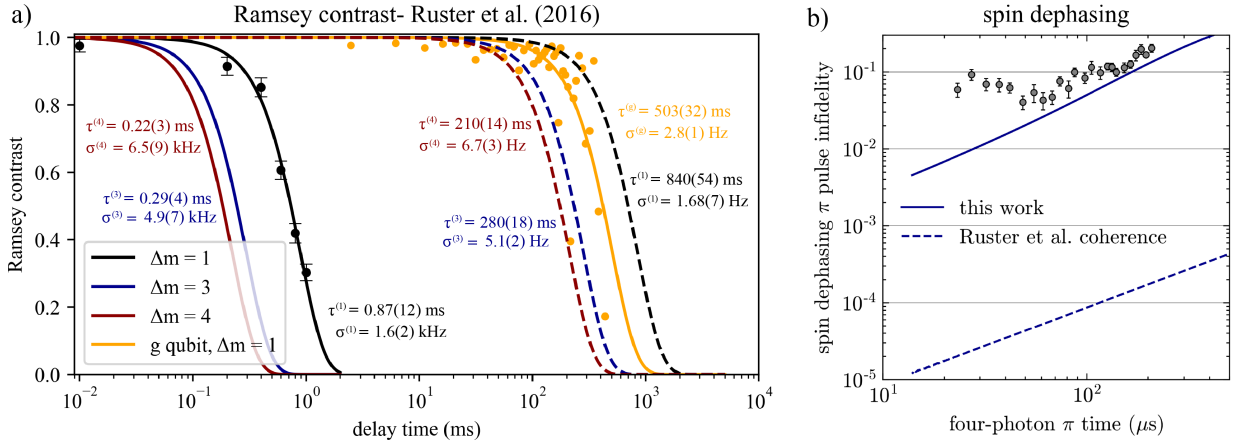


FIG. 18. **a)** (black circles) Ramsey contrast measured in the $D_{5/2}$ manifold in our experimental setup, with colored curves representing extrapolated coherences for larger Δm transitions within $D_{5/2}$. (orange circles) Ramsey contrast presented in Ref. [48] on a spin qubit in $S_{1/2}$, with dashed curves corresponding to expected contrast for transitions in the $D_{5/2}$, assuming the same noise sensitivity. **b)** Four-photon π pulse transfer infidelity due to spin dephasing, with magnetic field sensitivity in our experiment (solid) and the expected contribution assuming the experimental conditions of [48] (dashed).

Spontaneous Raman scattering

We estimate contributions to the π pulse transfer infidelity incurred by spontaneous Raman scattering via the $P_{3/2}$ manifold according to the model presented in [55] and verified in [56, 57]. For a π pulse we assume population spends equal time in each qubit state, and for the four-photon transition presented in the main text the incurred infidelity is

$$\epsilon_{srs} = \frac{\Gamma_0 + \Gamma_3}{2} t_g \quad (\text{H1})$$

where Γ_i is the scattering rate out of the state $|i\rangle$ as labeled in Fig. 1b and t_g is the π time of the transition. We use the beam waist and polarization parameters given in Table I. In Fig. 19a we plot the probability that a Raman scattering error occurred during the π pulse at different π times, corresponding to different R_\perp beam power. From branching ratios $\sim 94\%$ of scattering events leave the qudit manifold and scatter to either the $S_{1/2}$ or $D_{3/2}$ manifolds, both of which are bright under our fluorescence checks and can be detected and converted to an erasure error. The dashed line in Fig 19 corresponds to the probability of a Raman scatter error occurring that cannot be converted into an erasure error, where population has scattered back into the qudit subspace in the $D_{5/2}$ manifold.

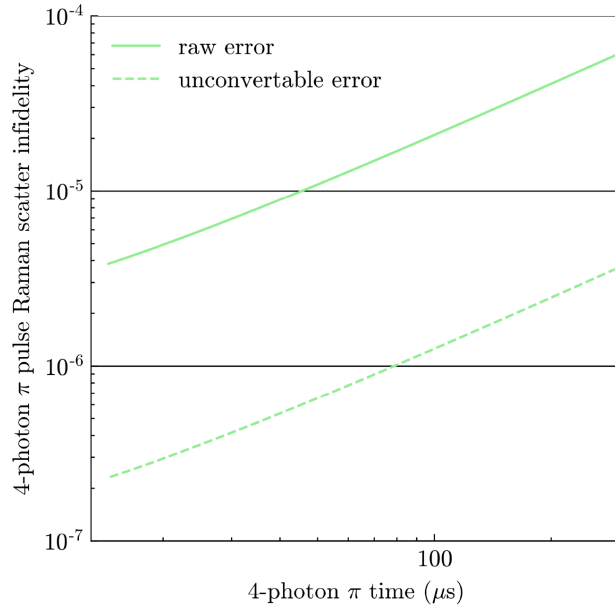


FIG. 19. **a)** Raman scattering errors during four-photon π pulse at different Zeeman splitting factor increases relative to this experiment. R_\perp beam is increased by the same factor to maintain the Rabi frequency, with P state detuning held constant. **b)** Raman scattering error except with P state detuning decreased by the square root of the B-field factor increase to maintain constant Rabi frequency. Dashed lines in both figures correspond to Raman scattering errors that cannot be converted to leakage errors via our fluorescence detection procedure.